Aaron W. Goodwin-Jones, Ricardo Cabrita, Mikhail Korobko, Martin Van Beuzekom, Daniel D. Brown, Viviana Fafone, Joris Van Heijningen, Alessio Rocchi, Mitchell G. Schiworski, and Matteo Tacca

Transverse mode control in quantum enhanced interferometers: a review and recommendations for a new generation

Optica, 2024; 11(2):273-290

DOI: http://dx.doi.org/10.1364/optica.511924

OPTICA

Transverse mode control in quantum enhanced interferometers: a review and recommendations for a new generation

AARON W. GOODWIN-JONES,[1,2,*] RICARDO CABRITA,[3] MIKHAIL KOROBKO,[4] MARTIN VAN BEUZEKOM,[5] DANIEL D. BROWN,[1,6] VIVIANA FAFONE,[7,8] JORIS VAN HEIJNINGEN,[3] ALESSIO ROCCHI,[8] MITCHELL G. SCHIWORSKI,[1,6] AND MATTEO TACCA[5]

[1]OzGrav, Australian Research Council Centre of Excellence for Gravitational Wave Discovery, Australia
[2]Department of Physics, University of Western Australia, Crawley 6009, Australia
[3]Centre for Cosmology, Particle Physics and Phenomenology, Université Catholique de Louvain, Louvain-La-Neuve B-1348, Belgium
[4]Institut für Quantenphysik und Zentrum für Optische Quantentechnologien der Universität Hamburg, Luruper Chaussee 149, 22761 Hamburg, Germany
[5]Nikhef, Science Park 105, 1098 XG Amsterdam, The Netherlands
[6]School of Physical Sciences, University of Adelaide, Adelaide, 5005, Australia
[7]University of Rome Tor Vergata, I-00133 Roma, Italy
[8]INFN, Sezione di Roma Tor Vergata, I-00133 Roma, Italy
*aaron.jones@ligo.org

Received 9 November 2023; revised 20 December 2023; accepted 21 December 2023; published 13 February 2024

Adaptive optics has made significant advancement over the past decade, becoming the essential technology in a wide variety of applications, particularly in the realm of quantum optics. One key area of impact is gravitational-wave detection, where quantum correlations are distributed over kilometer-long distances by beams with hundreds of kilowatts of optical power. Decades of development were required to develop robust and stable techniques to sense mismatches between the Gaussian beams and the resonators, all while maintaining the quantum correlations. Here we summarize the crucial advancements in transverse mode control required for gravitational-wave detection. As we look towards the advanced designs of future detectors, we highlight key challenges and offer recommendations for the design of these instruments. We conclude the review with a discussion of the broader application of adaptive optics in quantum technologies: communication, computation, imaging, and sensing.

https://doi.org/10.1364/OPTICA.511924

1. INTRODUCTION

Adaptive optics (AO) refers to any technology used to dynamically correct optical aberrations. Since its inception in the late 1970s [1], AO has played a pivotal role in various scientific and commercial applications. Possibly the most famous example of AO is the correction of atmospheric turbulence for astronomical telescopes [2,3]. The past two decades have seen the rapid development and commercialization of AO technology. As a result, AO is now also used in a wide variety of fields including free space optical communications (FSOC) [4–6], precision measurements [7,8], microscopy [9], and biological imaging [10].

Terrestrial gravitational-wave detectors (GWDs) [11] are exquisite optical systems. They use high optical powers and nearly perfect resonators to achieve a quantum-noise-limited sensitivity across their observing band. These km-scale interferometers are able to detect differential length changes of about $10^{-20}\ \mathrm{m}/\sqrt{\mathrm{Hz}}$ [12].

Active optical techniques were considered for GWDs as early as 1984 [13]. In 2003, researchers began attempting to directly translate astronomical AO techniques to Gaussian beams and GWDs [14]. However, deploying active optics in quantum enhanced instruments poses numerous technical challenges. Particular issues include back-scatter, polarization, vacuum, and low-frequency stability. In the past 20 years, the GW community along with many other independent researchers have developed bespoke sensing and actuation schemes that integrate adaptive optics into the precision engineered system. The resulting detectors are able to significantly suppress quantum noise at audio frequencies [15–17]. This achievement has required decades of development of AO.

To date, uptake of AO systems has generally been constrained to incoherent sources of light (e.g., [3,9,10]). In contrast, GWDs, FSOC, and many quantum optics applications generally use coherent light and spherical mirrors. The eigenmodes of these optical systems are Gaussian modes [18–21]. The more precise, but seldom used term "transverse mode control" refers to adaptive optics when applied to a system with discrete transverse eigenmodes (e.g., [22]). We provide a brief introductory summary of Gaussian modes in Supplement 1, Section A. Throughout this review, we generally consider the Hermite-Gaussian (HG) modes due to residual astigmatism in GWDs [23,24]. When used, Laguerre-Gaussian (LG) modes are defined with the radial index, p, following the azimuthal index, l, LG_{pl}. In Gaussian optics, the transverse properties of laser beams are described by a complex beam parameter:

$$q(z) = iz_R + (z - z_0), \tag{1}$$

where z_R is a scaling parameter describing how quickly the beam expands and z_0 is a positioning parameter describing where the beam radius reaches a minimum. The problem of ensuring that the complex beam parameter of the incoming light matches the complex beam parameter of the resonator is referred to as mode matching. Additionally, the HG modes describe only perfect spherical mirrors. However, any real optical system has surface figure errors and clipping. These effects shift the mode basis away from the analytical solutions given by the HG based model [25]. Instead, numerical models such as the linear canonical transform (LCT) or fast Fourier transform (FFT) must be used to compute the mode basis [25]. We refer to this as mode basis degradation.

Despite significant development in mode control, mode mismatch accounts for a substantial fraction of the optical loss budget in today's GWDs [16,17], thus limiting the reduction in quantum noise. Future detectors, envisioned to start operation in $\sim$2035 [26–28], will require higher levels of quantum-noise suppression, which will require a reduction in the static optical mismatch. Furthermore, they plan to operate with significantly increased optical powers. These optical powers introduce thermal transients, thus requiring better control of the dynamic mode mismatch. Therefore, it is required that wavefront control improves substantially over the next 10 years.

This paper is a historical review of the key developments in the field. In the interest of brevity, we assume some familiarity with GWDs; a complete introduction to the field, including all field-specific nomenclature, can be found in Supplement 1, Section B. Furthermore, a more detailed discussion of quantum noise and how it links to mode matching can be found in Supplement 1, Section C. Mismatch sensing schemes for Gaussian beams are summarized in Section 2. Then, we summarize in Section 3 the custom actuators designed to meet the demanding noise tolerances in opto-mechanics. In Section 4, we summarize the installed AO at the sites.

As quantum techniques begin to be used more generally, it will be critical to match both free space and fiber optical modes between resonators with minimal loss. In Section 5, we make recommendations on the use of the developed technology within GWD and speculate more broadly on applications within quantum information science.

A. 70 Years of Adaptive Optics

AO is the process by which optical aberrations are corrected by active elements. The simplest example is the use of a fast steering mirror (FSM) to maintain the alignment of a laser beam to a quadrant photodiode (QPD) in the presence of seismic or atmospheric turbulence. The technique is well developed with applications in astronomy, vision science, microscopy, and FSOC.

The first proposal for AO was from Babcock in 1953 [2]. Babcock suggested using a knife edge (see Supplement 1, Section D) to interrogate the beam and feed it back to an Eidophor (a precursor to modern spatial light modulators), which would spatially modulate the phase of the beam. Initially, the technique was focused on astronomical and defense applications to correct for atmospheric turbulence. In subsequent years several review articles were published [1,3]. One key development in AO is to use the Zernike polynomials [29] to describe the wavefront deformations. These wavefront deformations may be determined using a Hartmann sensor (e.g., [30]) with incoherent light from a distant stellar source. This can be corrected using a deformable mirror [31]. In astronomy, laser guide stars [32] are used to provide point spread functions to the telescope. For a thorough treatment, please see [31].

Since the development of AO for astronomy, several other fields have made use of the technology. For example, in vision science adaptive optics can be used to mitigate time-dependent imperfections in the lens of the eye and allow high-resolution photographs of the retina [10]. In astronomy a distinction is made between *active optics* and *adaptive optics*. Active optics refers to translational and rotational control of mirrors, whereas adaptive optics refers to higher-order effects. In microscopy, a similar approach can be used to overcome lensing by time-varying flows in the imaged medium [9]. A comparison and review of the work in the first three fields is presented in [33]. Recent work developing free space optical communication links has to overcome atmospheric turbulence [4].

2. PROPOSED MISMATCH SENSING SCHEMES

Several optical mode sensing schemes have been proposed that meet the requirements of GWDs. We group these into indirect methods—which image the effects of thermal transients, direct methods—which directly measure the mode matching between resonators, and mode decomposition—which attempts to decompose the beam and identify the mode structure and mode basis. However, prior to discussing mode sensing specifically, we will comment on the design considerations that minimize the need for modal actuation.

A. Design Considerations

The Rayleigh range of the eigenmode in the arms of the LIGO detector is $\sim$400 m [34]. As such, the mode matching between the input optics and arms cannot be corrected by distance optimization alone. Furthermore, given the size of the beams, it is not possible to profile the beam directly. Therefore, the designs of these telescopes [35–37] are critical to avoid static mismatches in the interferometer.

The designs of such telescopes typically use off-axis spherical or parabolic mirrors to avoid back-reflections from imperfect anti-reflective coatings. Such telescopes can be designed using spherical mirrors with angles that minimally couple astigmatism [38]. A thorough tolerance analysis is then undertaken in simulation to minimize the sensitivity to possible polishing errors. This must be done while also ensuring that the cavities are geometrically stable, thus strongly enforcing the modal basis and facilitating alignment control.

An alternative option, pursued by Advanced Virgo, is to use marginally stable recycling cavities. In this case, the high-magnification telescopes are shifted to the input optics [39]. The design of the input and output optics requires a similar tolerance analysis [40,41].

To date, GWDs have been designed to use spherical mirrors, thus enforcing the HG mode basis. However, a series of papers [42,43] followed by preprints [44,45] considered the use of non-spherical mirrors to reduce thermal noise. Recently, non-spherical mirrors have been proposed once more [46], to shift the resonance of higher-order modes away from degeneracy with the HG_{00} mode. The recycling cavities can then be designed by constructing an appropriate cost function and using Monte Carlo based simulations [46].

B. Indirect Mismatch Sensing Techniques

One of the crucial developments is an ultra-low-noise Hartmann wavefront sensor (HWS). These devices differ from the Shack-Hartmann sensors (e.g., [31]), common in other AO applications, as the micro-lens array is replaced with a plate of uniformly spaced pinholes, though the operating principle is the same. Forgoing the lenslet array allows for higher sensitivity as the effect of aberrations from imperfections in the lenses is removed, but also results in greatly reduced light collecting efficiency [30,47]. Both Advanced LIGO and Advanced Virgo use the HWS described in [30]. In the GWD implementation, probe beams of incoherent light are retro-reflected through transmissive optics and onto the HWS, as illustrated in Fig. 1. The measured distortions of these probe beams are, hence, related to distortions in the actual test masses themselves. The HWS can be calibrated to the cold mirror surface maps, which are measured independently. As the mirror thermally deforms, the HWS can then provide information on the current absolute mirror surface to a high precision.

The Hartmann sensor is an indirect method of sensing mismatch. The result contains information on the wavefront deformations, but contains no information on the overlap between the cavity eigenmode wavefronts and the injected wavefronts. In the case of gravitational wave detectors, the lensing that degrades mode matching is typically caused by temperature gradients due to optical absorption. Each test mass supports a number of vibrational eigenmodes, the spectrum of which depends on temperature, and thus another indirect mode sensing method is to track these eigenmode frequencies. This idea was first reported in [48].

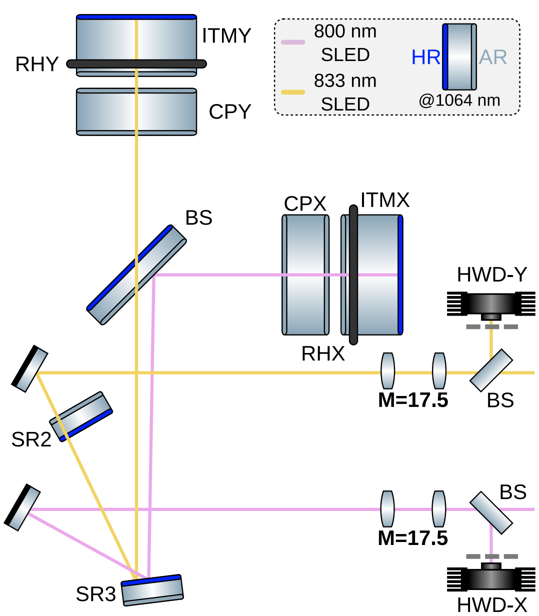

Fig. 1. Schematic representation of the Advanced LIGO wavefront sensors. SLEDs inject light at 800 nm (X-arm) and 833 nm (Y-arm). The AR coating on the BS reflects the 800 nm beam and transmits the 833 nm beam allowing for independent measurements of X and Y test masses. Ring Heater X (RHX) and RHY are actuators; see Section 3.A.1 for details. Adapted from [8] with permission.

C. Direct Mismatch Sensing Techniques

The most common way of inferring the laser beam parameter directly is to profile the beam. Common approaches include: the knife edge method, the chopper wheel, the scanning slit, and the camera method. Details of these methods can be found in Supplement 1, Section D. Additionally, for Advanced LIGO and Advanced Virgo, calibrated cameras are placed in the near and far fields of pick-off beams to track temporal changes in beam shape. For the core interferometer, these beams first pass through beam reducing telescopes, which may introduce systematic errors. Depending on the accumulated Gouy phase, deviations in this beam size can tell the GWD scientists, operators, and commissioners either about changes in w_0 or z_0. A similar approach is used for the Advanced LIGO input optics and further information can be found in [40].

For the input and output optics, single-digit-percent-level mismatching is achieved via traditional methods during commissioning. Once single-digit-percent-level mismatching is achieved, resonant methods must be used that directly interrogate the overlap of the incoming light and resonator eigenmode.

1. Resonant Wavefront Sensing

In the case of alignment sensing, the beat between reflected PDH sidebands and reflected HG_{01}/HG_{10} modes is routinely used to control the alignment of suspended cavities ([49,50] and therein). Since the HG modes are orthonormal, on a large area photodetector there would be no beat. However, a quadrant photodetector (QPD) breaks the orthonormality. Some segmented photodetectors are shown in Fig. 2 and a historical review of the alignment sensing developments between 1984 and today is provided in Supplement 1, Section E.

In the year 2000, Mueller and others proposed extending the resonant wavefront sensing used for alignment control, to mode matching control [51]. For a small mismatch in beam parameters, light will scatter from mode $HG_{n,m}$ into $HG_{n+2,m}$ and $HG_{n,m+2}$ with the amplitude coupling coefficient [51–53]:

$$k_{n,n+2} = \frac{\sqrt{(n+1)(n+2)}}{4}\left(\frac{i\Delta z - \Delta z_R}{\overline{z_R}}\right), \tag{2}$$

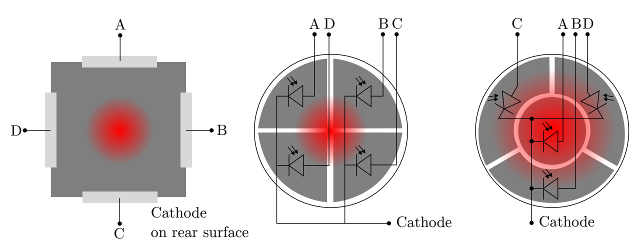

Fig. 2. Frequently used segmented and position sensing diodes. Active areas are shown in dark gray, metal contacts in light gray, and the beam is shown in red. Far left depicts a biased lateral effect position sensor, the middle depicts a quadrant photodiode, and the far right depicts a bulls-eye photodetector.

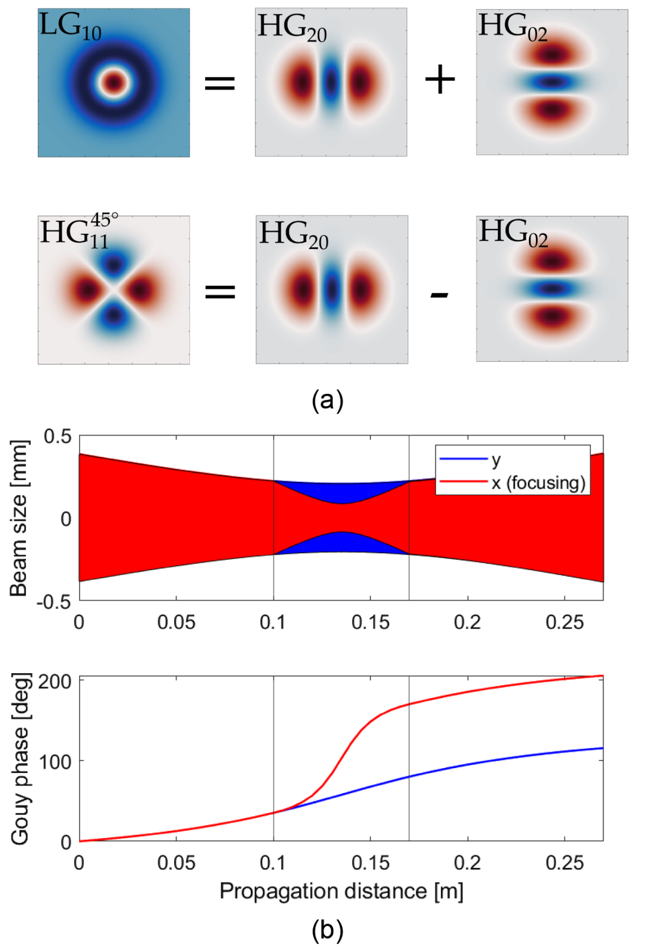

Fig. 3. Mode conversion can be used to make the LG_{10} mode detectable on a QPD. (a) Decomposition of the LG_{10} and 45° rotated HG11 in the HG basis. (b) Plot of the beam size and Gouy phase accumulation on the x and y axes as the beam travels through a mode converter.

$$\therefore \quad k_{0,2} = \frac{1}{2\sqrt{2}} \left(\frac{i\Delta z - \Delta z_R}{\overline{z_R}} \right), \tag{3}$$

where Δz denotes the difference in waist position, Δz_R the difference in Rayleigh range, $\overline{z_R}$ the mean of the two Rayleigh ranges, and n, m are mode indices. If the mode mismatch is reasonably anastigmatic then scattering will occur equally into HG_{02} and HG_{20} modes. The result is equal to a doughnut shaped LG_{10} mode [54–56], as illustrated Fig. 3(a). Therefore, a bulls-eye photodetector (BPD), shown schematically in Fig. 2, breaks the orthonormality. Thus a beat occurs between the LG_{10} mode and the reflected HG_{00} cavity locking sidebands. By using two BPDs, separated by an appropriate Gouy phase, it is possible to simultaneously gather information on Δz and Δz_R. While promising, the technique has not been widely accepted by the community. BPDs are difficult to source; furthermore, overlapping requirements on the accumulated Gouy phase and beam radius at the BPD mean that, likely, a custom BPD is required.

2. Mode Conversion

One option is to sidestep the BPD requirement by converting the LG_{10} mode associated with mode mismatch into a HG_{11} *pringle* mode, which is more convenient for detection with a QPD. Because both HG and LG modes form a complete basis to describe laser beam modes, one can decompose LG_{10} into a combination of two HG modes: HG_{20} and HG_{02} [54,55,57]. Additionally, a 45° rotated HG_{11} mode can also be decomposed in the same combination of HG modes, minus a sign flip, as shown in Fig. 3(a). So, in principle, by adding a $\pi/2$ phase shift along one axis, it is possible to convert LG_{10} into a 45° rotated HG_{11}. In order to do this, the Gouy phase shift is exploited.

Generally, this is done using two cylindrical lenses to create a confined region where the beam is astigmatic. Provided the lenses are positioned so that the beam is no longer astigmatic outside of the converter, the additional Gouy phase shift along the astigmatic axis remains constant after the converter and subsequent detection is possible on a QPD. Consider a beam (along the non-focusing axis) with Rayleigh range, z_R, and beam-waist position, z_0. The desired Gouy phase shift will be achieved with cylindrical focal length [54]:

$$f = \frac{z_R}{1 + 1/\sqrt{2}}. \tag{4}$$

This lens must be placed at $z^{\pm} = z_0 \pm f\sqrt{2}$ to mode match the output beam while achieving the Gouy phase shift. Figure 3(b) shows the beam size in the astigmatic and non-astigmatic axis, and the evolution of the Gouy phase shift for a mode converter using cylindrical lenses. Mode converters with the same principle have also been realized using spherical mirrors at a 45° angle [58].

Typically, mode converters are used in conjunction with heterodyne techniques to generate an error signal for mode mismatch. In [59,60], frequency-shifted sidebands in the HG_{00} mode beat against the converted HG_{11} on a QPD to generate an error signal. By placing a beam splitter and two sets of QPDs separated by 45° in Gouy phase, it is possible to get separate error signals for waist size and waist position mismatch, respectively [59]. Such a mode converter set-up is currently being used to mode match the filter cavity for frequency-dependent squeezing at Advanced Virgo [61].

One limitation of the mode converter is that it assumes a LG_{10} mode and is thus incompatible with astigmatism. The frequency-dependent source uses curved mirrors in off-axis telescopes in order to reduce optical losses [38], causing some small astigmatism by design. This astigmatism limits how much mode matching can be achieved with the current mode converter [61].

3. Radio Frequency Beam Modulation

Mode conversion is under active investigation, and is a promising technique for future gravitational-wave detectors. However, it suffers from three key limitations. First, it is not trivially generalized to sensing the coupled cavity mismatch. Second, it requires Gouy phase telescopes. Finally, it requires several new sensors and pick-offs to be introduced into the vacuum envelope. In 2017, reference was first made to the RF beam shape modulation method in an alignment sensing paper [62]. In 2020, the first RF beam modulation proposal paper was published [53]. The premise is to generate a frequency offset beam-shape modulation using an acousto-optic modulator (AOM) and a phaseplate. Using the nomenclature defined in Supplement 1, Section B, the carrier is at $HG^{\omega_0}_{0,0;q_1}$ and the modulation is at $HG^{\omega_0+\Omega}_{2,0;q_1} + HG^{\omega_0+\Omega}_{0,2;q_1}$. Considering only the n modes, where the beam experiences a basis change, we obtain

$$\mathrm{HG}^{\omega_0}_{0;q_1} \rightarrow \quad k_{0,0}\mathrm{HG}^{\omega_0}_{0;q_2} + k_{0,2}\mathrm{HG}^{\omega_0}_{2;q_2} + \mathcal{O}(\Delta z^2, \Delta z_R^2), \quad (5)$$

$$\mathrm{HG}^{\omega_0+\Omega}_{2;q_1} \rightarrow k_{2,2}\mathrm{HG}^{\omega_0+\Omega}_{2;q_2} + k_{2,0}\mathrm{HG}^{\omega_0+\Omega}_{0;q_2} + k_{2,4}\mathrm{HG}^{\omega_0+\Omega}_{4;q_2} + \mathcal{O}(\Delta z^2, \Delta z_R^2), \quad (6)$$

where $k = k(\Delta z, \Delta z_R)$ denotes a coupling coefficient, defined in Eq. (2). Further values of k can be found in [53]. On a photodiode where the beam radius is much smaller than the active area, only modes of the same order will produce beat notes due to the orthogonality of the HG modes. Therefore, in the presence of a mismatch, there will be a beat with frequency Ω and the two mode-matching quadratures z and z_R can be read out with appropriate choices of demodulation phase.

The scheme as proposed for LIGO is shown in Fig. 4. The $\mathrm{HG}^{\omega_0+\Omega}_{2,0;q_1} + \mathrm{HG}^{\omega_0+\Omega}_{0,2;q_1}$ mode is generated from the coherent locking field (CLF) [63–65], which passes through the optical parametric oscillator (OPO) that generates the squeezing. The mode sensing field then co-propagates with the squeezing until it is reflected by the OMC. This proposal requires only a single new component—the phaseplate, since all other components exist.

In contrast to generating the modulation with an AOM and phaseplate, several authors have begun exploring the possibility of using an electro-optic lens. First mentioned in [62], initial results were shown by two independent groups in 2020 [66,67]. Proof-of-principal work was presented in 2023 [68] and the applicability of the schemes to higher-order carrier modes is discussed in [69].

Another approach is to forego the phaseplate and inject only the frequency offset beam, thus relying on the mode mismatch to excite the higher-order mode. For example, consider the field $\mathrm{HG}^{\omega_0+\Omega}_{0,0;q_1}$; when the beam experiences a basis change, we obtain

$$\mathrm{HG}^{\omega_0+\Omega}_{0;q_1} \rightarrow k_{0,0}\mathrm{HG}^{\omega_0+\Omega}_{0;q_2} + k_{0,2}\mathrm{HG}^{\omega_0+\Omega}_{2;q_2} + \mathcal{O}(\Delta z^2, \Delta z_R^2). \quad (7)$$

On transmission of the cavity, the auxiliary modulation is filtered away leaving only $\mathrm{HG}^{\omega_0}_{0;q_2}$ and $\mathrm{HG}^{\omega_0+\Omega}_{2;q_2}$. In general, these do not produce a beat as they are different modes; however, on a finite area photodiode or on a BPD a beat note will be produced. The

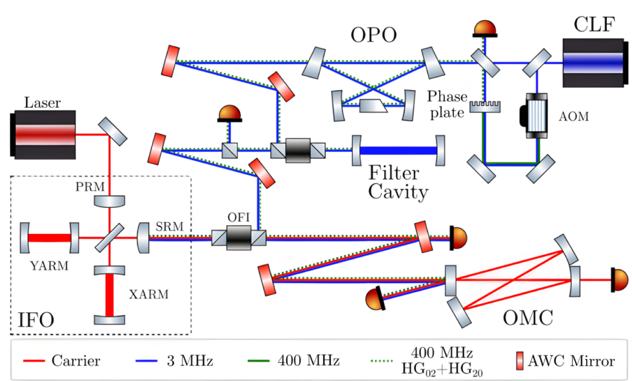

Fig. 4. Suggested implementation of a RF beam shape modulation in a gravitational-wave detector. The modulation is generated with an AOM and phaseplate; it then co-propagates with the squeezed light until the OMC. At the OMC it is reflected and the mode-matching can then be inferred. Reprinted with permission from [53], © The Optical Society.

scheme is an extension of the 1984 Anderson alignment sensing proposal [13] and was recently published [70]. Furthermore, by observing on transmission, there is the possibility of developing a scheme directly sensitive to the mismatch between cavities [70]. However, the mode separation frequency of the second cavity must be within the FWHM of the first cavity. The $\mathrm{HG}^{\omega_0+\Omega}_{0;q_1}$ sideband is then resonant in the first cavity. On a mismatch between the cavities it scatters into the $\mathrm{HG}^{\omega_0+\Omega}_{2;q_2}$ mode with complex amplitude given by Eq. (2). This technique is powerful as it is the first direct measure of mode mismatch between coupled resonators. Some proof-of-principal work has been carried out at LIGO Livingston [71].

D. Beam Decomposition

The previous section deals entirely with matching the complex beam parameter of an incoming light field to the complex beam parameter of a resonator. However, mirror surface roughness [72], parametric instability [73], and thermal transients can all degrade the mode basis [25]. These degradations shift the mode basis away from the ideal HG one, which is only valid for infinite diameter, perfect, spherical mirrors in free space.

In this abstract space, two figures of merit are important. First, the overlap between the input laser eigenmode and the resonator eigenmode, which dictates the power in cavity and, thus, the shot noise level of the detector; second, the overlap between the squeezer eigenmode and the resonator eigenmode. This overlap dictates the maximum possible quantum enhancement. These two things must be optimized without causing resonances that lead to instabilities.

In the remainder of this section, we will review two key ideas. The first is the phase camera, a Cartesian decomposition of the wavefront, referenced to some characteristic beam. The second is to decompose the beam into some known reference basis, using either an optical convolution or reference cavity.

1. *Phase Cameras*

Phase camera is the name colloquially given to devices that perform radio-frequency differential wavefront sensing at significantly higher spatial resolution than can be achieved with segmented photodiodes. The namesake relates to their ability to produce image maps of the transverse amplitude and phase of optical beats between frequency-shifted beams. By contrast, Hartmann wavefront sensors measure only the combined wavefront and segmented PDs can usually measure only one mode.

There exist principally five designs of phase cameras, which differ in their approach to measuring the spatial profile of the optical heterodyne field. The first, and most natural design would be a high-element-number PD array, where each element is simultaneously demodulated at the desired frequency. However, the typical frequency offset for a GWD sideband is 1–100 MHz and so cross-talk between the elements poses challenging limits on the bandwidth and performance of these devices. The three most developed designs of phase cameras are highlighted in Fig. 5, and the following paragraphs discuss each of these individually.

Scanning pinhole phase cameras. The first phase camera was developed to image the differential wavefront of the GWD sidebands compared to the carrier [74]. In the first demonstration [75], a frequency offset reference beam was combined with the test beam on a beam splitter. The field was then reflected from a pair of

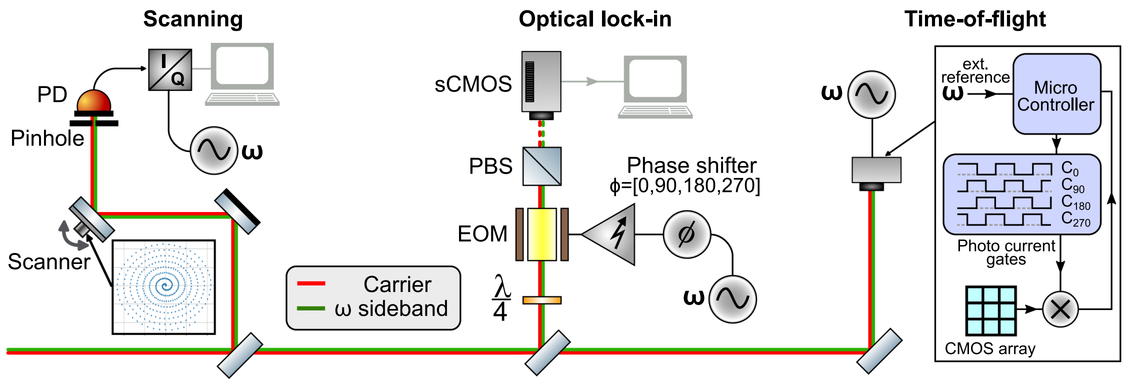

Fig. 5. Schematics of the scanning, optical lock-in, and time-of-flight phase camera designs. Not shown is the external reference beam, which is required when individually measuring the sideband field(s), rather than measuring the beat of the carrier and sideband field, which is as shown here.

galvanometer-driven steering mirrors onto a pinhole photodiode. By demodulating the photodiode signal at the difference between the reference field and the test fields, phase and amplitude maps could be obtained of the carrier and sidebands independently.

In the first applications of the phase camera [74,76], the reference field was no longer used. Instead, by demodulating at the difference between the sideband and carrier frequency, phase and amplitude maps could be obtained of the sideband referenced to the carrier wavefront. The technology was very mature and has been used to study the mode structure of initial LIGO [77] and assist with commissioning the initial LIGO OMC [74,76].

The scanning phase camera has seen significant development since the first proposal. Modern cameras simultaneously image 11 sidebands (upper and lower sideband at five demodulation frequencies plus the carrier). Each image has 2^{14} pixels, with maximum phase resolution $\sim\lambda/1600$ (at the center of the beam) acquired in under a second [78]. In contrast to the first version, the cameras can scan either the test beam, or both beams over the pinhole. They make use of high-dynamic-range ADCs, fast FPGAs, and calibrated actuators to achieve this resolution. Due to the slow scanning speed when compared to environmental phase fluctuations, this resolution is only achievable for differential phase images between carrier and sidebands. See [78] and references therein for further details. This style of phase camera is routinely used in the Virgo GWD [79]. There, differential phase images are preferentially obtained to mitigate phase fluctuations in the reference beam fiber and also the residual motion of the benches themselves.

Optical lock-in phase camera. Optical lock-in phase cameras use amplitude modulation to optically demodulate the RF beat down to ~100 Hz where it can be measured with a standard CCD camera. The amplitude modulation is achieved with a Pockels cell and waveplates, which first modulate the polarization, and a polarizing beam splitter (PBS) that converts this into amplitude modulation. The Pockels cell is driven at the desired sideband frequency, with large voltages ~1 kV being required to achieve adequate modulation depths. Amplitude and phase maps are acquired by subsequently stepping the phase of the amplitude modulation through $\phi = [0, \pi/2, \pi, 3\pi/2]$ and recording images. The four images taken are then digitally processed into amplitude and phase maps.

The technique was proposed in [80], where a 2 Mpx camera is used to produce images with sensitivity up to −62 dBc after 2 s of averaging. Subsequently, the camera has been trialed at LIGO [81] and used to image parametric instabilities [82], thus determining the mode of the PI. Further work has explored using neural networks to determine the mode decomposition of the beam [83]. However, the camera can only image one sideband at a time. Future integration work will need to consider stable and efficient generation of the large driving voltage (~1 kV) at tunable frequencies, with minimal RF contamination of the laboratory environment.

Time-of-flight phase camera. Time-of-flight (ToF) cameras (e.g., [84]) are a mature technology used in many augmented reality products, including smartphones and video games. The operating principle is that a set of infrared light emitters turn on at $t = T_0$ and off at $t = T_1$, and the cycle repeats at T_2. Four quadrants of a pixel are triggered to collect charges at four different phases between the T_0 and T_2. By taking the ratio of the charges collected in each pixel, the distance can be estimated. A distance L can only be measured unambiguously provided as long as it does not exceed the wavelength of the modulation, $L < c(T_2 - T_1)/2$.

ToF cameras were proposed as phase cameras by the Advanced Virgo team (Section 7.7.1.3 in [85]). The light is discarded and the quadrants of each pixel are clocked at the frequency difference between the sideband and the carrier, similar to the optical demodulation approach. This means that only one spectral component can be interrogated at a time. Up to 100 MHz demodulation with −62 dBc has been demonstrated [86].

Spatial light modulator based phase cameras. Spatial light modulator based phase cameras tag each pixel on a reference beam with an orthogonal code [87]. The code is imprinted on the reference beam with a spatial light modulator (SLM). This reference beam is combined with a test beam on a beam splitter, which can be focused onto a single photodiode. By demodulating photodiode data, with the code for a particular pixel, information is obtained on the phase and amplitude of the beat note for that pixel. For a SLM with 9 pixels, nine concurrent demodulations must take place. Further work is required to adapt the scheme to image the sidebands in a terrestrial GWD.

Summary. Table 1 compares the performance of the current most developed types of phase cameras. For further details on using phase cameras to measure mode mismatch, see [88].

2. *Modal Weighting*

Since both the HG and LG modes are orthonormal and form a complete basis, any electric field can be described by

Table 1. Phase Camera Parameter Comparison[a]

	Scanning	Optical Lock-In	Time-of-Flight
Pixels (px)	128 × 128	2048 × 2048	320 × 240
Frame rate (fps)	1 (max. 10)	10 (max. 100)	max. 60
Sensitivity (dBc/px)	−61 (at 1 fps)	−62 (at 0.5 fps) −72 (120 × 128 px, 1 fps)	−62 (at 1 fps) −50 (at 7 fps)
Detectable beam diameter change (%)	2.3	0.15	1.1
Spatial precision (mode weight ppm)	16500	1100	7800
Phase RMSE (nm)	0.7	Not available	0.1
Maximum frequency	250 MHz	100 MHz	100 MHz
Num. demodulations	11	1	1

[a]The values presented were extracted or derived from [78–80,86], respectively. The detectable beam diameter change assumes a telescope to image the beam onto the camera. Assuming the beam diameter on the camera is 1/3 of the aperture, the detectable change is 3/(Num. Pixels). Spatial precision is computed from the spot size change using Eq. (2). The sensitivity for the scanning phase camera was computed taking into account the optimal power in the reference beam [79].

$$E(\vec{r}, t) = \sum_{n,m,j} a_{n,m,j} u_{n,m} \exp(i\omega_j t), \quad (8)$$

where $u_{n,m}$ denotes either the HG or LG mode. The process of determining the parameter $a_{n,m,j}$ for a given electric field is called modal weighting.

Diagnostic breadboards. One of the options to determine the modal weights is to perform a mode scan. To perform the mode scan, a special optical resonator is assembled that should be stable, with clear separation between different modes. Usually, a cavity like the LIGO pre-mode cleaner is used [89]. Kwee *et al.* developed a diagnostic breadboard based on the pre-mode cleaner, which was able to perform the mode weighting along with measurement of the beam pointing and relative intensity noise [90]. This method was successfully used in 2015 to characterize thermal lensing in various materials [91] and has inspired follow-on work in the FSOC community [92]. However, it is only possible to obtain the mode power, $|a_{n,m,j}|^2$, rather than the complex mode weight.

In 2010, Takeno *et al.* developed an extension to the diagnostic breadboard approach, where the phase and amplitude of deviations from a perfect Gaussian mode could be imaged. The result is a phase camera that processes only deviations from the carrier mode [93].

Spatial filters. An alternative approach is to use a spatial filter to compute the fraction of light in a particular mode. This is achieved by passing the beam through a basic optical convolution processor (BOCP), consisting of a phaseplate, lens, and aperture, all separated by the lens focal length, as illustrated in Fig. 6. It is possible to show, by application of the Rayleigh-Sommerfeld equation, that the on-axis intensity is equal to

$$I(0, 0, z_{\text{PD}}) \approx \frac{\exp(i(2kf + \pi/2))}{f\lambda} \times \int\int_{-\infty}^{\infty} E(\xi, \eta, z_{\text{Phaseplate}}) T(\xi, \eta) \mathrm{d}\xi \mathrm{d}\eta. \quad (9)$$

Such a derivation may be found in many places (e.g., §3.1 [94]). If $T(\xi, \eta) = u^*_{\bar{n},\bar{m}}(\xi, \eta)$, then, since the HG and LG modes are orthonormal, the on-axis intensity is proportional to the power in the $\bar{n}$, $\bar{m}$ mode:

$$I(0, 0, z_{\text{PD}}) \propto a^2_{\bar{n},\bar{m}}/f^2\lambda^2. \quad (10)$$

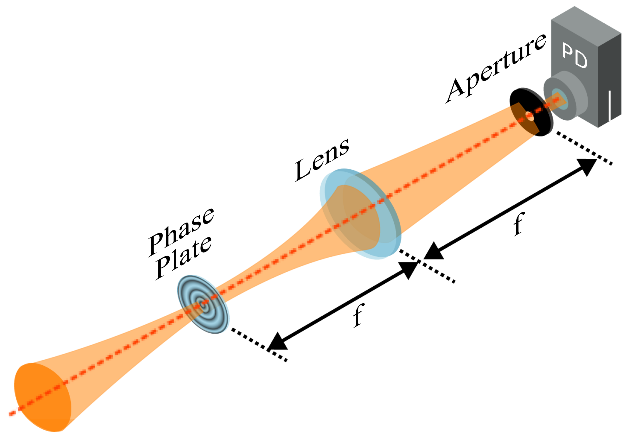

Fig. 6. Mode weighting with a spatial filter. An incoming electric field $E(\xi, \eta)$ is passed through a phase modulating plate, with transmission function $T(\xi, \eta)$. In the far field the on-axis intensity is proportional to the overlap integral of T and E.

f denotes the focal length of the lens and we have implicitly assumed the light is monochromatic (e.g., [95]). This idea was first proposed by Golub in 1982 [96].

However, difficulty fabricating the photographic plates led to a slow adoption of spatial filters [97]. Approximate amplitude modulation can be achieved on a phase-only device by varying the depth of a blazed grating [98], thus eliminating the need for a separate mask. This, combined with the popularity of liquid crystal based spatial phase modulators [99], led to a resurgence in the technology [100]. A more rigorous technique for amplitude modulation was developed by Bolduc *et al.* [101]. Another approach is to use *computer generated hologram correlation filters* [102]. Computer generated holograms are now popular and there exists a dedicated review on the topic [97] along with an earlier text [103], to which the reader is referred for further general information.

Within the gravitational-wave community, mode weightings at the part-per-million level are required. A thorough tolerance analysis of spatial filters found that the mode precision is limited by: a) the relative positioning accuracy and b) finite aperture effects. These cause cross-coupling of unwanted modes [95]. Overcoming these limitations resulted in a mode (power) weighting precision of 4000 ppm. Further investigation used a meta-material spatial filter to achieve a mode (power) weighting precision of 0.6ppm/$\sqrt{\text{Hz}}$ [104]. The optical apparatus was fully integrated into the LIGO

Table 2. Comparison of some of the Direct Sensing and Mode Decomposition Technologies[a]

	Precision [Mode Weight]	Integration	Tested in GWD
Spatial filter	$0.6\ \text{ppm}/\sqrt{\text{Hz}}$ [104] 4000 ppm (RMS) [95]	To LIGO CDS [104]	No
Diagnostic breadboard	20 ppm (RMS) [90]	Complete	All
Phase cameras	1000 ppm (1 Hz) [Table 1]	Complete	LIGO, Virgo
Resonant wavefront sensing	15000 ppm [51]	Complete	LIGO
Radio frequency beam modulation	100 ppm (RMS) [53]	No	No

[a]Conversion from fractional waist radii to mode weight is obtained from Eq. (2).

Control and Data System. Further work on back-scatter and longitudinal tolerance analysis are required before spatial filters could be integrated within a GWD.

E. Summary of Sensing Technologies

In this section, we have reviewed several different schemes for sensing eigenmode mismatch. GWDs use a careful design procedure informed by the simulation to ensure their optical telescopes will achieve high magnification while also ensuring insensitivity to small radii of curvature errors. This is complemented by Hartmann cameras that image the thermal deformations of the main optics. Several technologies have been proposed and trialed for direct mode sensing, including resonant wavefront sensing, mode conversion, and radio frequency beam modulation. Additionally, several technologies have been proposed for beam decomposition including: phase cameras, diagnostic breadboards, and spatial filters. We present a comparison in Table 2.

3. PRECISION ACTUATION OF SPATIAL QUANTUM STATES

The required actuation on mirror radii of curvatures in advanced GWDs ranges from $\sim$100 μD on the test masses [8] to $\sim$100 mD on the input and output optics [105]. Many adaptive optics technologies already exist, but are unsuitable for use in a GWD. Requirements on scattered light exclude many mirror technologies. For example, spatial light modulators are excluded by wide-angle scatter caused by the pixel grid. It is challenging to polish ultra-thin mirrors to meet the scatter requirements and this excludes many unimorph (e.g., [106]), monomorph (e.g., [107]), and various bimorph (e.g., [108,109]) mirrors. Mirrors must be suspended from complex seismic isolation chains to suppress phase noise and thermal noise and this excludes many mechanical and piezo-actuated mirrors due to vibrations, phase-flicker, and $1/f$ noise (e.g., [87,110,111]). Finally, vacuum outgassing requirements exclude many commercial solutions.

The gravitational-wave community has coalesced around three sets of solutions. First, for the core interferometer, transmissive optics are radiatively heated to introduce thermal lensing. Second, the input path must survive high optical powers and so transmissive (or reflective with the HR surface after the substrate) optics are heated by direct thermal contact. Lastly, the output path has ultra-low-loss and phase noise requirements, so reflective optics, which are mechanically stressed, are used.

A. Core Interferometer

Within the core interferometer, we will review four approaches used to develop appropriate radiative heating patterns on the optic.

1. Ring Heaters

Ring heaters were discussed as early as 2002 [112] and first tested at the GEO600 observatory [113]. These ring heaters can be used to compensate for thermal lensing and also to correct for small radii of curvature errors. While thermal lensing mainly occurs at the center of a mirror, because that is where the laser beam deposits its energy, the ring heater heats the outside barrel of a mirror. Figure 7 illustrates the concept.

Fused silica has both a positive refractive index change with temperature, $dn/dT > 0$, and a positive coefficient of thermal expansion, $dL/dT > 0$. For the ITM, the recycling cavity eigenmodes are affected by both dn/dT and dL/dT. The arm cavity eigenmode is only affected by dL/dT on both test masses. Therefore the heating at the edge creates a more convex mirror, offsetting the central heating caused by absorption of the Gaussian laser beam. The heaters are made of two Pyrex rings surrounded by a polished copper shield, which reflects the radiation onto the test mass. The Pyrex ring is heated from a conductive wire wrapped around [8,114,115].

Because the ring heater acts by reducing the thermal gradient, it can only induce a reduction of the radius of curvature of a mirror. For a typical fused silica mirror with a nominal radius of curvature around 1.5 km, the ring heater at maximum power is able to reduce the radius of curvature by 100 m ($\sim$100 μD) [8,114].

A variant of the GEO600 ring heater is also used on the signal recycling mirror 3 (SR3) in Advanced LIGO. In this instance, a ring behind the test mass causes a thermal expansion of the outer edges of the mirror, thus making SR3 more convex [116].

In Advanced Virgo, ring heaters have been installed also to tune the radii of curvature of the recycling mirrors (both PR and SR) and of the optics the filter cavity for the injection of the squeezing [114].

Recently, Richardson *et al.* have investigated extending the use of the ring heater concept to the front surface of the test mass.

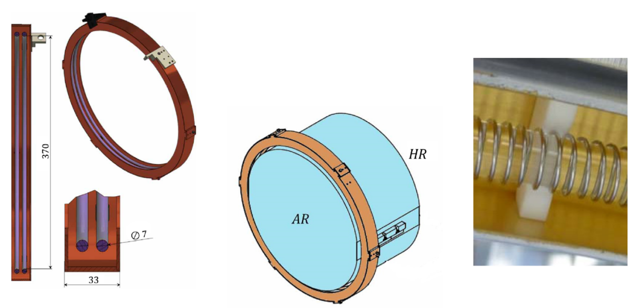

(a) (b) (c)

Fig. 7. Ring heaters. (a), (b) Reproduced from [114] under the CC-BY-4.0 License. (c) Reproduced with permission from [8], © The Optical Society. (a) Drawings for the ring heater in Advanced Virgo. (b) Depiction of ring heater around test mass. (c) Photograph of a ring heater installed in Advanced LIGO.

Referred to as a front surface type irradiator (FROSTI), it would allow a non-spherical radius of curvature to be created by thermally tuning a spherical optic [117], thus changing the resonance condition of very-high-order optical modes, as discussed in Section 2.A.

2. Central Heating Radius of Curvature Correction

Peripheral heating solutions like ring heaters can only reduce the radius of curvature. While this allows to compensate for thermal effects (thermo-optic and thermo-elastic), there may be situations where it is necessary to increase the radius of curvature of an optic, for example, to compensate for deviations from nominal specifications. The central heating radius of curvature correction (CHRoCC) projects a heat pattern onto the center of an optic, increasing the radius of curvature. The device is a black body emitter inside a heat shield, together with an ellipsoidal reflector used to project the heat into the target optic [118].

It was initially proposed and developed to correct the radius of curvature of the end test masses in enhanced Virgo. The change of the radius of curvature of the mirrors shifts the resonance frequency of higher-order modes, which were otherwise degenerate with the fundamental mode, causing locking instability issues [118]. In this instance, the dynamic range was almost 1000 m change in the radius of curvature. Currently, these CHRoCC devices have been installed to increase the tuning possibilities of the power and signal recycling mirrors in Advanced Virgo.

3. CO_2 Lasers and Compensation Plates

Shortly after the GEO600 demonstration of a ring heater [113], compensation plates were proposed [112,119] and tested at the High Optical Power Test Facility, Gingin, Australia [120]. The premise is to install a dedicated optic, with strong optical path length change with temperature. One concept was to use materials where either $dn/dT < 0$ or $dL/dT < 0$ ([121] and therein). This has been successfully implemented for Faraday isolators in GWDs [122,123]. However, as Zhao explains [124] it was difficult to find suitable materials for use in a cavity.

The interferometer is much less sensitive to noise on the CP than noise on the test mass, and so actuation can be much stronger [125]. For example, in the first proposal, a conductive ring heater was glued onto the compensation plate, which would not be possible on the test mass. However, in later revisions, this was swapped for a powerful CO_2 laser [126]. The CO_2 emits at a wavelength of 10.6 μm, which is strongly absorbed by fused silica. The absorbed light changes the optical path length through the material and tuning the intensity of the laser adjusts the change to optical path length [8,115]. In aLIGO, the CP was initially polished flat [127] and then re-polished with some focal length offset [128].

The CO_2 laser and CP can be used as either a positive or negative lens [8,115]. When shining a Gaussian beam at the center of the compensation plate, the temperature rises in the middle and the radius of curvature of the optic is increased. This mode of operation is called central heating.

In Advanced Virgo, the aberrations due to the average coating absorption, which are mostly radially symmetric, are corrected for by shining two annuli-shaped ring patterns on the compensation plates. The optimal compensation heating pattern was estimated using a FEA simulation [85]. These two ring-shaped intensity patterns are obtained with two axicon lenses. A combination of waveplates and lenses is used to control the intensity and thickness of each ring, respectively. This set-up is called the Double Axicon System (DAS) [115].

Finally the CO_2 laser can also be used in combination with a scanning system [112,129], to compensate for non-axi-symmetric aberrations. The beam is moved with a constant speed over the compensation plate and the intensity is adjusted for each location according to a correction map. Additionally, work is ongoing at Virgo [130] to use the modified Gerchberg-Saxton algorithm [131] and a commercially available deformable mirror to shape the CO_2 laser beam and develop novel heating pattern beams.

4. Matrix Heaters

Matrix heaters are arrays of heaters that can illuminate a heating pattern onto the test masses. This heating pattern deforms the optic surface, leading to the enhancement or suppression of particular optical modes. The first proposal [132] was to use 9×1 cm $\times$ 1 cm pixels operating between 500° and 1200°C. The proposal suggested placing this outside the vacuum system and imaging it onto the test mass using a ZnSe lens. The heating pattern could then be used to tune problematic higher-order-mode resonances in the arm cavities. One of the study's coauthors then developed a thorough optimization procedure that could be used to minimize wide-angle scatter caused by mirror surface roughness [133].

The first demonstration of a matrix heater [134] was at GEO600; 198 individually addressable heating elements were arranged on a PCB. The heating elements could dissipate 1 W at around 600°C ($\lambda \gtrsim 4$ μm). In this instance, the imaging apparatus consisting of a ZnSe vacuum window is used along with a parabolic aluminum mirror.

The matrix heater concept has been further developed at Virgo [135,136], to cope with localized heating from highly absorbing regions of the test mass, with a characteristic size of about 100 μm, known as point absorbers [137]. These absorbers cause scattering of power from the fundamental mode to higher-order modes in the arm cavities, thus increasing the round-trip losses. The peculiarity of the Virgo solution is that the corrective pattern is produced through the use of a binary mask illuminated by a single heating element. This allows to greatly simplify the driving electronics and to increase the spatial resolution of the actuator, being equivalent to a 40×40 array of heaters. The mask is then imaged onto the test mass using a germanium lens and ZnSe vacuum window.

B. Input Path

The idea to place some smaller active optical elements in the vacuum system naturally arises following the development of the compensation plates. The initial design for aLIGO had provision for two adaptive optical elements [40]. The design was similar to the initial compensation plate. In this instance, a circular aperture SF57 substrate was used as a lens [138]. This lens was held in place by four segmented metal clamps in thermal contact with the barrel of the optic. The clamps were heated by a resistive wire wrapped around the clamp. The substrate was polished to be flat on both sides; by heating the clamps the optical path length on the edge of the mirror could be increased, and thus, a negative lens could be formed with dynamic range $f \geq 10$ m [139]. The transfer function was stable, with a unity gain frequency of around 20 mHz, DC gain of around 100, and it did not significantly degrade the beam quality [140]. By actuating each quadrant independently, tilt and astigmatism could be introduced into the output [138]. However, the optic was never installed as the mode matching in the input optics was never considered a performance limitation [141]. Furthermore, there were concerns about excessive heat on the table interfering with the seismic isolation [139]. 200 mD of actuation was achieved with 10 W of heating [142]. The work is summarized in [142].

The idea can be expanded by using a mirror and placing the AR surface at the front and the HR surface at the back. In this way, the beam passes through the substrate twice. On the HR surface, a multielement heating array can be bonded. An initial proposal used nine heating elements and found minimal hysteresis and excellent linearity [143]. 64 mD of focal length actuation was achieved with only 160 mW, reducing the thermal load on the isolated tables. Meanwhile promising results were shown for astigmatism actuation. In the 2013 proposal [144], 61 heaters were used, enabling the correction of Zernike modes up to fifth order.

C. Output and Squeezing Path

The output and squeezing paths of current GWDs require ~90% [145] mode matching to ensure excellent quantum efficiency between the cavity used to generate the squeezing, filter cavity, interferometer, and output mode cleaner (e.g., [146,147]). This path has similar requirements to the input path. However, instead of high-power handling, requirements exist on back-scatter, phase noise, and loss. As noted in [148], these requirements justify a new class of solutions such as thermally actuated bimorph mirrors, with high dynamic ranges. The operating principle is that a 6 mm thick mirror is inset into an aluminum ring. The inner diameter of the aluminum ring is smaller than the outer diameter of the mirror, and thus applies a compression bias. The compression bias crushes the mirror to be more convex. As the mirror is heated, the compression bias is decreased. Further work is ongoing to demonstrate concave mirrors and larger diameters [149].

The excellent noise characteristics of the thermally actuated mirror make it ideal for use in the GWD output paths. However, for the filter cavity paths, it was required to dither the radii of curvature at $\mathcal{O}$(1–10 Hz). Since the unity gain frequency of the thermally actuated mirrors is $\mathcal{O}$ 1 mHz, a new technology was required for the filter cavity path. The adopted solution is a carefully engineered piezoelectrically actuated mirror. The design uses preloading and a custom flexure to convert the stress from the piezo into a spherical deformation while meeting the aLIGO noise requirements [150].

4. APPLIED MISMATCH MITIGATION STRATEGIES

A mathematical derivation of dynamics of thermal issues in gravitational-wave test masses was published in 2009 [151]. Summaries of the thermal compensation systems in the core interferometer of Advanced Virgo were published in 2011 [7], 2019 [115], and 2023 [114]. A summary of the thermal compensation system in the core interferometer of Advanced LIGO was published in 2016 [8]. In this article, we will briefly summarize the sensing schemes and actuation channels that are routinely used throughout the entire interferometer in both LIGO and Virgo.

A. Input Optics

The active optics for the input optics is a critical subsystem, as higher-order modes can mediate the transfer of noise into the GWD readout. For alignment, resonant wavefront sensing (see Supplement 1, Section E) is routinely used. Actuation is then provided by coil-magnet actuators ([152] and therein).

For sensing the beam waist position and radius diagnostic, calibrated cameras are placed in the near and far fields of the beam [40]. These cameras are placed between the IMC and PRC, to track the eigenmode in the IMC. This eigenmode will change as IMC heats up. In addition, pick-off photodiodes in the input path and PRC monitor the power recycling gain. The power recycling gain depends on mode matching efficiency among other things.

Section 3.A.3 discussed the idea of optics with a negative optical path length change with respect to temperature. This was not used for compensation plates; however, the Faraday isolators in the GWD input optics do contain a thermally driven positive lens [122].

B. Squeezed Light Injection and Interferometer Output Path

Active optics on the squeezed light and interferometer output paths are critical to realizing high levels of quantum noise suppression. All the techniques specified in the previous section are used.

There are various options to sense the mode matching between the interferometer and OMC. One commonly used approach is to partially lock the interferometer and use the OMC as a diagnostic breadboard (Section 3.D.2). However, there are several issues. For example, the output beam contains many sidebands and junk light, which contaminates the measurement of mode matching. Additionally, the length sensing and control scheme for the full interferometer requires the OMC to be locked; therefore the state of the interferometer during the OMC scan does not represent the state used for gravitational wave detection.

Another useful measure is the complex transfer function between the test masses motion and displacement readout [71]. Maximizing the gain of this transfer function indicates high optical power in the arm cavity and, thus, good mode matching. However, without linear error signals, this cannot be automated. Furthermore, the function depends on many interdependent parameters and cannot be uniquely constrained to mode matching.

For the squeezed path, the squeezing level into the interferometer and the audio diagnostic field [65] are used to infer the squeezing mode matching. In terms of actuators, both thermally and piezoelectric actuated bimorph mirrors are used (Section 3.C). However, as with the transfer function method, it cannot trivially be automated and requires substantial commissioning time to diagnose issues.

C. Core Interferometer

Within the core interferometer, it is exceptionally challenging to define a mode basis. Despite efforts to produce perfect spherical mirrors, effects such as point absorbers [137], apertures, and surface figure errors shift the mode basis away from the HG basis. This leads to a shift in the accumulated Gouy phase. The problem is further complicated by thermal transients that add a time-dependent Gouy phase change. The Gouy phase change can bring unwanted modes onto resonance, destroying the sensing and control schemes.

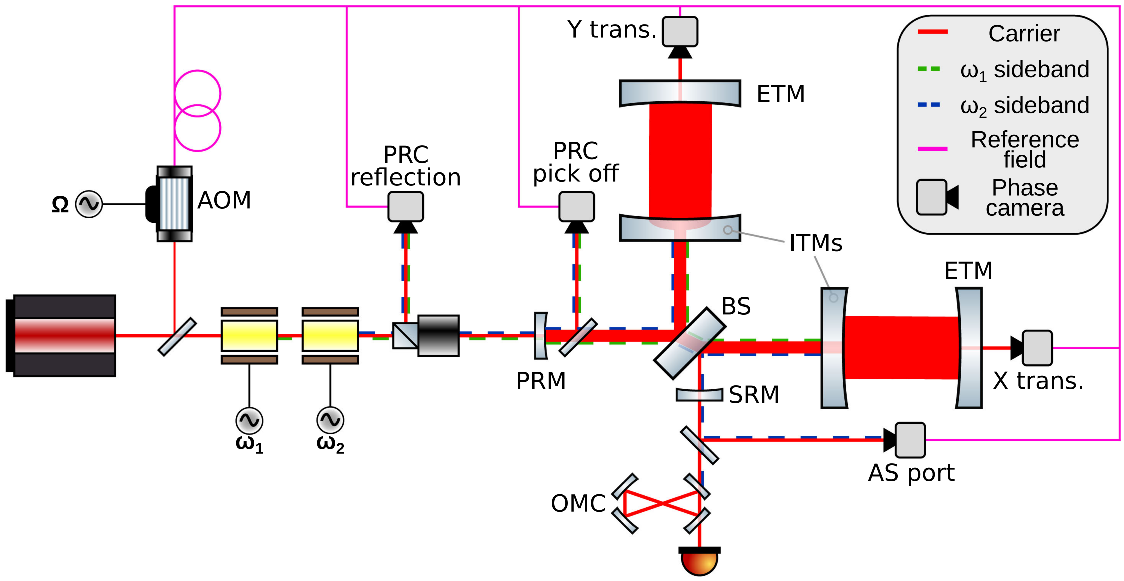

Fig. 8. Possible phase camera locations and schematic diagram of phase cameras in a GWD. In Advanced Virgo, cameras are installed at the PRC pick-off and AS port.

At the time of writing, current detectors use a variety of tools to infer to the desired operating point. The complex transfer method described above is frequently used. In addition, maximizing the power recycling gain and scans of the arm cavities are also used to infer the state. However, at LIGO the only dedicated mode sensing actuator is the Hartmann sensor. The Hartmann sensor is only sensitive to changes in the thermal state and does not offer a quantitative decomposition of the mode content in the arms. Thus, it is not possible to clearly identify higher-order-mode resonances throughout the core interferometer, nor it is trivial to extract mode sensing error signals for automatic mode matching. Actuation is provided by: the ring heaters, compensation plates, and SR3 heater.

At Virgo, the use of marginally stable recycling cavities amplifies the sensitivity to mode mismatch. In addition to the methods above, Virgo makes routine use of scanning pinhole phase cameras. Two of these devices are currently installed, the first one at the output port of the interferometer and the second one on a pick-off beam extracted in the PRC. Figure 8 shows a schematic diagram of the phase cameras in a GWD. Another phase camera is planned in reflection of the PRC in the future. In the Virgo implementation, a frequency-shifted reference beam is obtained from a pick-off in the main laser beam. The pick-off is fiber-coupled to the phase camera installation. The shifted reference beam is useful for differentiating the upper and lower sidebands, which is useful as sideband imbalance is known to cause issues in the locking of cavities [153]. However, phase noise along the path of the optical fiber, during the measurement time ($\sim$1 s), limits the accuracy of the phase measurement allowing, nowadays, only differential phase measurements between carrier and sidebands. Some optical fiber phase noise cancellation techniques are under test to be implemented in future upgrades in order to be able to independently measure the absolute phase of the different beams (carrier, and upper and lower sidebands). Moreover, the information provided by the images acquired by the phase cameras have been used to estimate the mode content of the carrier beam at the output of the interferometer [154], giving inputs on the actuation needed to reduce the resonance of higher-order modes in the FP cavities. An optimization of the data processing of the phase camera images is in progress with the aim of estimating the mode content of all the acquired beams. This will help in the evaluation of the mismatch level in the various cavities of the GWDs.

5. FUTURE REQUIREMENTS

Two next-generation GW detectors are anticipated to be operational around 2035: Cosmic Explorer (CE) in the US [155] and Einstein Telescope (ET) in Europe [26]. In addition, we anticipate the routine use of integrated quantum photonics to produce vast entangled networks [156], imaging below the shot noise level (e.g., [157]), and define SI units [158]. In this section we will begin by reviewing the challenges faced by future GWDs; we will then discuss the work required to integrate the mode sensing solutions described in Section 2 into these detectors. Lastly, we will close with a discussion on how this work could be applied outside the field of GWD.

A. Future Requirements for Gravitational-Wave Detectors

ET will be an underground facility, hosting three pairs of interferometers, each 10 km long with 200 kg test masses. Each pair will contain a low-frequency (ET-LF) and high-frequency detector (ET-HF). The reference design for ET-LF is a cryogenic detector with mirrors at 10 K and only 18 kW of optical power in the arms. The reference design for ET-HF is to operate at room temperature with 3 MW of optical power in the arms.

CE is a conceptual design for a 40 km long detector with 1.4 MW of optical power and 320 kg test masses. The reference design for CE is a singular, broadband interferometer with the potential to build a 20 km second interferometer, possibly in the southern hemisphere [27]. There exists scope for a potential upgrade to CE, referred to as CE2, which may integrate longer wavelength lasers and cryogenic silicon optics. Both CE and ET can operate independently or as part of a global network, enabling unprecedented cosmological reach and high detection rates [27].

Several intermediate detectors and prototypes have been proposed to bridge the technological gap between the current and future detectors. Current detectors have around 40 kg, room temperature test masses with around 300 kW of optical power. One intermediate detector is the Neutron Star Extreme Matter Observatory (NEMO), which uses 4.5 MW of stored optical power and 70 kg mirrors at around 130 K mirrors [28]. Another is the LIGO Voyager project, which proposes 3 MW of optical power with 50 kg, 123 K mirrors [159]. The cryogenic community is supported by several prototypes [160–163].

The Virgo project is developing Advanced Virgo Plus, Phase II [164], which uses 100 kg room temperature mirrors and will operate in the 5th Observing Run. The LIGO community is currently using the term A# to refer to the upgrade in the LIGO vacuum enclosure, following the 5th Observing Run. This will likely involve heavier test masses, 10 dB of squeezing, and 1.5 MW of stored optical power in the arms [165]. The Virgo community is using the term Virgo_nEXT for a similar upgrade [166]. The larger test masses may suppress many radiation-pressure-mediated angular instabilities ([167] and references therein), therefore enabling higher power operation. Furthermore, larger test masses may permit larger beam sizes, reducing coating thermal noise [151].

B. Semi-Classical Mode Sensing and Control Challenges in Future Detectors

These changes required by future detectors will have several important effects on the interferometer modes.

First, the free spectral range of the longitudinal resonance of arm cavities is close to the detection band, around 3.8 kHz for CE and ∼15 kHz for ET. This means that the majority of higher-order modes are within the detection bandwidth. Even while operating on the fundamental mode, Brownian motion on the test mass scatters light into higher-order modes. As such, when within the detection bandwidth, their control and suppression are significantly more difficult.

When a high overlap is achieved between a mirror mechanical mode and an optical mode, the optical mode can become resonant at a frequency offset. The radiation pressure may then drive the mechanical mode, causing the system to become unstable. The effect is referred to as parametric instability (PI, e.g., [168] and therein), and the parametric gain depends on the optical power and accumulated Gouy phase, among other things. As the stored power increases, the effects of PI will become more severe [169]. Furthermore, as higher-order modes are brought into the detection band PI will be harder to control. As such it will be critically important to minimize scatter into higher-order modes and avoid PI amplification.

Future detectors will likely use larger diameter test masses. These large dimensions will put strict requirements on the polishing of the optical elements. Surface figure errors over the large area of the test mass contribute to shifts away from the HG mode basis, thus making an analytic description of the interferometer state intractable.

High powers in the interferometer will lead to large transient thermal effects in mirror substrates, especially in the central beam splitter. This is especially true for ET-HF and CE, which use fused silica and operate at room temperature. In the current generation of detectors, this time-dependent mismatch has caused numerous problems. For example, by changing the mode shape and basis in the recycling cavities, the resonance conditions for the control sidebands in the first-order HG modes are shifted. Since these sidebands are used for angular sensing and control, changing resonance conditions introduces additional noise into the detector. Additionally, a changing mode basis means the PI gain becomes time-dependent and substantially complicates PI mitigation. Lastly, differential changes in the mode basis couple laser frequency noise into the interferometer output signal, further limiting sensitivity. Given these constraints, the current detectors are able to operate using ∼1 W of ring heater power [170] and limiting to ∼300 kW arm power (e.g., [171–173]).

A comprehensive study of the actuator requirements for further increases in LIGO arm power has been carried out [174] and it was determined that increasing arm power will require increased ring heater and CO_2 power as well as potential new actuators such as FROSTI.

For cryogenic detectors, the thermal conductivity of crystalline silicon at ∼100 K is ∼900 W/m K [175]. In contrast, the thermal conductivity of fused silica at room temperature is ∼1 W/m K (e.g., [176,177]). When used for laser mirrors, the effective thermal conductivity of cryogenic silicon is slightly increased [178]. A trade-off study on cryogenic suspensions for high-power GWDs found that geometric distortions will be suppressed by several orders of magnitude compared to their room temperature counterparts [179].

C. Challenges on the Way to 10 dB Squeezing

Both ET and CE reference designs require 10 dB of quantum noise suppression to reach design sensitivity. In order to suppress both quantum shot noise at high frequencies and quantum radiation pressure noise at low frequencies, quantum uncertainty has to be squeezed in different quadratures at different signal frequencies. Such frequency-dependent squeezing is achieved by reflecting squeezed light off a filter cavity [145,180–183]. Reaching 10 dB of squeezing requires the total optical loss to be less than 10% in the full detection band. There are several sources of squeezing degradation, such as direct optical loss in the filter cavities and the detector, scattering loss, length and phase noises, coupling two quadratures of squeezed light, and, importantly, mode mismatch (e.g., [15–17,184]). The overall effect of mode mismatch would have to remain at a level below ∼1 % (p. 120 [26] and §8.3.5 [27]).

Mode mismatch affects squeezing level in two distinct ways: as the direct source of optical loss, and as an additional degradation due to a dephasing mechanism [146,147,184]. In this mechanism, the squeezed vacuum coherently couples into a higher-order mode and then back into the signal mode after acquiring some (unknown) phase. Due to this additional phase, the back-coupled light contributes a part of anti-squeezed quadrature into the squeezed mode, thereby degrading it. The coupling phase depends on the specifics of the coupling mechanism, and the detector needs to be optimized with respect to it.

For CE and ET-HF, the large beam radius will require significant focusing, likely before and possibly also after the central beam splitter [37]. This focusing will incur a significant Gouy phase shift between different HOMs. Various imperfections along the propagation path, most notably due to thermal effects on the central beam splitter, will introduce an additional unknown coupling phase between different HOMs, thus contributing to the dephasing mechanism and leading to a significant reduction on squeezing beyond the direct loss.

ET-LF is planned to operate in a detuned regime, where the opto-mechanical interaction between the light and test masses causes an additional resonant signal enhancement for a range of signal frequencies; the resulting quantum noise level is thus rather complex. Filter cavities are required to replicate the quadrature rotation caused by the interferometer. As such, the filter cavity arrangement for ET-LF is commensurately complex requiring either two filter cavities (Section D.3 of [185]) or one coupled filter cavity [186], to achieve the required quadrature rotation. The dephasing mechanisms will cause significant degradation at the frequencies around the optomechanical resonance by coupling a large portion of anti-squeezing into the signal mode. This will require limiting the amount of squeezing injected into the detector, thus impacting the overall sensitivity.

D. Recommendations

We identify three clearly separable issues in future room temperature GWDs, first, the coupling of optical states between resonators, especially in the recycling cavities, output optics, and squeezing optics. Optimal mode matching is difficult to achieve by indirect methods due to basis mismatches. For this reason, we recommend the use of one of the direct mismatch sensing schemes (Section 2.C), to be included in the baseline design of future interferometers. In addition to the direct correction, squeezed HOMs can be employed to further improve the sensitivity [147,187].

Second is the issue of the mode basis degradation in the core interferometer, caused by point absorbers, marginally stable cavities, and higher-order effects. Without a clear understanding of the mode basis, it is not possible to understand the transient behavior of the full interferometer. For this reason, we recommend the use of a dedicated beam-decomposition technology to be included in the baseline design for future detectors. Furthermore, we note that future detectors may need actuators able to make non-spherically symmetric wavefront corrections, in order to mitigate higher-order effects.

Lastly is the issue of the transient behavior of the interferometer. Both Hartmann sensors and other more novel approaches would be able to image the transient behavior. However, additional work is required to develop new actuators to manage the transient thermal distortions in future detectors, as discussed further in [188,189].

For cryogenic detectors, further work is required to understand the requirements on actuation. Depending on the design of the recycling cavities, it may be possible to leverage the experience obtained from KAGRA as the detector moves to higher powers. For cryogenic detectors operating at 2000 nm wavelength, neither silicon nor InGaAs photodetectors have suitable responsivity. Extended InGaAs photodetectors are widely available and so mode sensing solutions requiring photodetectors can be reworked for this wavelength. However, technologies requiring quadrant or bullseye photodetectors, or cameras, may be prohibitively expensive, depending on wider market conditions.

E. Beyond Gravitational-Wave Detectors

Photonic states have a broad range of applications. In this section, we will review a collection of applications and how the mode sensing technologies could be used to further these areas of research.

One area with particular synergies is quantum information technology. The recent rise of photonic quantum computation [190,191], where squeezed modes provide the resource for creating large-scale entanglement [192,193], requires extremely high levels of mode-matching and precise mode shape manipulation [194]. Building extended quantum networks with quantum computers (not only photonic) requires secure and efficient quantum state transport between different nodes. This is enabled by (continuous-variable) quantum key distribution (QKD) (e.g., [195]) and quantum teleportation (e.g., [156]). Given the fixed loss per unit length of modern communication fibers, it is likely that such links will involve, at least, one free space component to a satellite receiver (e.g., [156]). However, atmospheric turbulence adds a temporally fluctuating mode basis shift, which may be corrected with the AO (e.g., [196]). This is similar to the temporal basis shift caused by thermal effects in the interferometer, which degrades the coherent and squeezed states in the interferometer. As such, these applications could benefit from the direct mismatch sensing schemes discussed in Section 2.C. Depending on the application, such research may also benefit from applying the ultra-low-phase-noise actuators discussed in Sections 3.B and 3.C to avoid mixing quantum states.

Several authors have considered the use of higher-order spatial modes to further enhance communication bandwidths [197,198]. As shown in [199], the fidelity with which the optical state must be matched depends strongly on the mode order. This area is analogous to matching a laser beam to an optical resonator and therefore many of the technologies discussed in Section 2 can be applied directly.

Several quantum technologies have proposed using higher-order transverse modes to reduce their noise. For example, in the area of optical clocks, higher-order modes have been proposed to reduce thermal noise [200] or avoid point defects (e.g., [201]). Then, in the area of cavity assisted atomic interferometry [202,203], higher-order modes can be used to increase the size of the beam and, thus, capture more atoms. Finally, in the field of optical tweezers increasing higher-order mode indices corresponds to increasingly steep potentials [204], leading to improved trapping. In all of these cases, switching to a higher-order transverse mode will lead to increased mode matching requirements [199]. In all three cases, matching to an optical resonator is required and as such many of the sensing and actuation schemes could be applied. In particular, the RF sensing schemes discussed in Section 2.C.3 have commensurately stronger error signals [69] and could be used to optimally match the beam into these cavities. This could reduce the linewidth of cavities in optical clock experiments, capture more atoms in atomic physics experiments, and increase the strength of the potential in optical tweezer experiments.

Quantum imaging technology can benefit from higher-order modes in several ways. First, entangled spatial modes allow higher resolution and lower noise in conventional imaging approaches [205–207]. However, so far these applications were limited by the ability to create, control, and detect quantum correlations in higher-order modes. Recent success in generating [207–210] and observing [211,212] of such states opens the way for their practical use, assuming they can be efficiently controlled. A second application in quantum imaging is the super-resolution approach, where higher-order modes are used to extract additional phase information and enable sub-diffraction imaging [213–215].

6. SUMMARY

AO is one of the most important optical techniques with a wide variety of applications. Gravitational-wave physicists applied active optics as early as 1985 and applied AO as early as 2003. Following nearly three decades of development, AO has been successfully translated to the Gaussian laser optics domain. With the introduction of frequency-dependent squeezing in Observing Run 4, we are seeing the routine use of AO to overcome quantum noise in a practical application.

In this review, we grouped mode sensing solutions into three categories: indirect mismatch sensing, direct mismatch sensing, and beam decomposition/basis identification. For each area, we have summarized the state-of-the-art mismatch sensing technologies and carried out a historical review of the technology to date.

We have further grouped actuators into three categories by area of application: first, the core interferometer, which requires handling $\sim 10^6$ W of optical power, ~ 100 μD actuation ranges, and ~ 10 cm optics; second, the input path, which must handle ~ 100 mD actuation range and ~ 100 W of optical power; finally, the output path requires ~ 1 W of optical power, ~ 100 mD actuation range, and variable bandwidth and actuation noise requirements. For each category, we have presented several solutions that meet the requirements and indicated which ones are currently in use.

The current detectors have employed a number of technologies to reach as much as 6 dB of shot noise suppression without introducing additional QPRN and maintaining ~ 300 kW of circulating power. In Section 4, we summarized the use of resonant wavefront sensing, diagnostic measurements, phase cameras, and actuators to achieve this result.

Future gravitational-wave detectors will require exquisite control of the spatial properties of the wavefront to avoid a plethora of issues. In Section 5, we have summarized these requirements and discussed the range of proposed solutions that could be employed to resolve them. We closed with a discussion of how this technology could be translated into a plethora of domains from laser communications to quantum sensing and the authors look forward to a bright future of enhanced adaptive quantum optics.

Funding. Australian Research Council (CE170100004, DE230101035); Fonds De La Recherche Scientifique-FNRS (4.4501.19); Deutsche Forschungsgemeinschaft (390833306); Nederlandse Organisatie voor Wetenschappelijk Onderzoek (162).

Acknowledgment. The authors are grateful to their LIGO, Virgo, and KAGRA collaboration colleagues for helpful discussions and their contributions to the detectors. Specifically, we wish to thank our LIGO PnP and Virgo DRS reviewers for their careful proofreading and feedback. We are indebted to the anonymous reviewers and editors at Optica for their thoughtful feedback. We thank Vaishali Adya, David Gozzard, and Carl Blair for helpful discussions. This document has been assigned LIGO Document Number P2300282 and Virgo Document Number VIR-0769A-23. A.W.G. acknowledges the LIGO Scientific Collaboration Fellows program for supporting their research at LIGO Livingston Observatory.

Disclosures. The authors declare no conflicts of interest.

Data availability. No data were generated or analyzed in the presented research.

Supplemental document. See Supplement 1 for supporting content.

REFERENCES

1. J. W. Hardy, "Active optics: a new technology for the control of light," IEEE Proc. **66**, 651–697 (1978).
2. H. W. Babcock, "The possibility of compensating astronomical seeing," Publ. ASP **65**, 229 (1953).
3. A. Glindemann, S. Hippler, T. Berkefeld, *et al.*, "Adaptive optics on large telescopes," Exp. Astron. **10**, 5–47 (2000).
4. L. B. Stotts and L. C. Andrews, "Adaptive optics model characterizing turbulence mitigation for free space optical communications link budgets," Opt. Express **29**, 20307–20321 (2021).
5. C. Chen, A. Grier, M. Malfa, *et al.*, "Demonstration of a bidirectional coherent air-to-ground optical link," Proc. SPIE **10524**, 120–134 (2018).
6. S. F. E. Karpathakis, B. P. Dix-Matthews, D. R. Gozzard, *et al.*, "High-bandwidth coherent optical communication over 10.3 km of turbulent air," Appl. Opt. **62**, G85 (2023).
7. A. Rocchi, E. Coccia, V. Fafone, *et al.*, "Thermal effects and their compensation in Advanced Virgo," J. Phys. Conf. Ser. **363**, 012016 (2012).
8. A. F. Brooks, B. Abbott, M. A. Arain, *et al.*, "Overview of advanced LIGO adaptive optics," Appl. Opt. **55**, 8256–8265 (2016).
9. N. Ji, D. E. Milkie, and E. Betzig, "Adaptive optics via pupil segmentation for high-resolution imaging in biological tissues," Nat. Methods **7**, 141–147 (2010).
10. M. Pircher and R. J. Zawadzki, "Review of adaptive optics oct (AO-OCT): principles and applications for retinal imaging [invited]," Biomed. Opt. Express **8**, 2536–2562 (2017).
11. B. P. Abbott, "Prospects for observing and localizing gravitational-wave transients with advanced LIGO, advanced Virgo and KAGRA," Living Rev. Relativity **21**, 3 (2018).
12. A. Buikema, C. Cahillane, G. L. Mansell, *et al.*, "Sensitivity and performance of the advanced LIGO detectors in the third observing run," Phys. Rev. D **102**, 062003 (2020).
13. D. Z. Anderson, "Alignment of resonant optical cavities," Appl. Opt. **23**, 2944–2949 (1984).
14. E. Calloni, J. T. Baker, F. Barone, *et al.*, "Adaptive optics approach for prefiltering of geometrical fluctuations of the input laser beam of an interferometric gravitational waves detector," Rev. Sci. Instrum. **74**, 2570–2574 (2003).
15. J. Lough, E. Schreiber, F. Bergamin, *et al.*, "First demonstration of 6 db quantum noise reduction in a kilometer scale gravitational wave observatory," Phys. Rev. Lett. **126**, 041102 (2021).
16. M. Tse, H. Yu, N. Kijbunchoo, *et al.*, "Quantum-enhanced advanced LIGO detectors in the era of gravitational-wave astronomy," Phys. Rev. Lett. **123**, 231107 (2019).
17. F. Acernese, M. Agathos, L. Aiello, *et al.*, "Increasing the astrophysical reach of the Advanced Virgo detector via the application of squeezed vacuum states of light," Phys. Rev. Lett. **123**, 231108 (2019).
18. A. G. Fox and T. Li, "Resonant modes in a maser interferometer," Bell Syst. Tech. J. **40**, 453–488 (1961).
19. H. Kogelnik and T. Li, "Laser beams and resonators," Appl. Opt. **5**, 1550–1567 (1966).
20. A. Siegman, *Lasers* (University Science Books, 1986).
21. C. Bond, D. Brown, A. Freise, *et al.*, "Interferometer techniques for gravitational-wave detection," Living Rev. Relativity **19**, 3 (2017).
22. L. M. Osterink and J. D. Foster, "Thermal effects and transverse mode control in a Nd:YAG laser," Appl. Phys. Lett. **12**, 128–131 (2003).
23. B. Sorazu, P. J. Fulda, B. W. Barr, *et al.*, "Experimental test of higher-order laguerre-gauss modes in the 10 m glasgow prototype interferometer," Classical Quantum Gravity **30**, 035004 (2013).
24. C. Bond, P. Fulda, L. Carbone, *et al.*, "Higher order Laguerre-Gauss mode degeneracy in realistic, high finesse cavities," Phys. Rev. D **84**, 102002 (2011).
25. A. A. Ciobanu, D. D. Brown, P. J. Veitch, *et al.*, "Modeling circulating cavity fields using the discrete linear canonical transform," J. Opt. Soc. Am. A **38**, 1293–1303 (2021).
26. H. Lueck, and ET Steering Committee, "Et design report update 2020," Tech Report (Einstein Telescope, 2020).
27. M. Evans, R. X. Adhikari, C. Afle, *et al.*, "A horizon study for cosmic explorer: science, observatories, and community," arXiv, arXiv:2109.09882 (2021).
28. K. Ackley, V. B. Adya, P. Agrawal, *et al.*, "Neutron star extreme matter observatory: a kilohertz-band gravitational-wave detector in the global network," Pub. Astron. Soc. Aust. **37**, e047 (2020).

29. F. von Zernike, "Beugungstheorie des schneidenver-fahrens und seiner verbesserten form, der phasenkontrastmethode," Physica **1**, 689–704 (1934).
30. A. F. Brooks, T.-L. Kelly, P. J. Veitch, *et al.*, "Ultra-sensitive wavefront measurement using a Hartmann sensor," Opt. Express **15**, 10370–10375 (2007).
31. F. Roddier, M. Séchaud, G. Rousset, *et al.*, *Adaptive Optics in Astronomy* (Cambridge University, 1999).
32. C. D'Orgeville and G. J. Fetzer, "Four generations of sodium guide star lasers for adaptive optics in astronomy and space situational awareness," Proc. SPIE **9909**, 99090R (2016).
33. K. M. Hampson, R. Turcotte, D. T. Miller, *et al.*, "Adaptive optics for high-resolution imaging," Nat. Rev. Methods Primers **1**, 68 (2021).
34. J. Aasi, B. P. Abbott, R. Abbott, *et al.*, "Advanced LIGO," Classical Quantum Gravity **32**, 115012 (2015).
35. M. Arain and G. Mueller, "Design of the advanced LIGO recycling cavities," Opt. Express **16**, 10018–10032 (2008).
36. M. Granata, M. Barsuglia, R. Flaminio, *et al.*, "Design of the Advanced Virgo non-degenerate recycling cavities," J. Phys. Conf. Ser. **228**, 012016 (2010).
37. S. Rowlinson, A. Dmitriev, A. W. Jones, *et al.*, "Feasibility study of beam-expanding telescopes in the interferometer arms for the Einstein telescope," Phys. Rev. D **103**, 023004 (2021).
38. P. Hello and C. N. Man, "Design of a low-loss off-axis beam expander," Appl. Opt. **35**, 2534–2536 (1996).
39. C. Buy, E. Genin, M. Barsuglia, *et al.*, "Design of a high-magnification and low-aberration compact catadioptric telescope for the Advanced Virgo gravitational-wave interferometric detector," Classical Quantum Gravity **34**, 095011 (2017).
40. R. Martin, P. Fulda, D. Feldbaum, *et al.*, "IO mode matching diagnostics on the IOT tables," LIGO technical document T1300941-v1 (LIGO Laboratory, 2014).
41. L. McCuller, S. Biscans, and L. Barsott, "Frequency dependent squeezing final optical layout," LIGO technical document T1900649-v8 (LIGO Laboratory, 2020).
42. E. D'Ambrosio, "Nonspherical mirrors to reduce thermoelastic noise in advanced gravitational wave interferometers," Phys. Rev. D **67**, 102004 (2003).
43. E. D'Ambrosio, R. O'Shaugnessy, K. Thorne, *et al.*, "Advanced LIGO: non-Gaussian beams," Classical Quantum Gravity **21**, S867 (2004).
44. R. O'Shaughnessy, S. Strigin, and S. Vyatchanin, "The implications of Mexican-hat mirrors: calculations of thermoelastic noise and interferometer sensitivity to perturbation for the Mexican-hat-mirror proposal for advanced LIGO," arXiv, arXiv:gr-qc/0409050 General Relativity and Quantum Cosmology e-prints (2004).
45. E. D'Ambrosio, R. O'Shaughnessy, S. Strigin, *et al.*, "Reducing thermoelastic noise in gravitational-wave interferometers by flattening the light beams," ArXiv, arXiv:gr-qc/0409075 General Relativity and Quantum Cosmology e-prints (2004).
46. J. W. Richardson, S. Pandey, E. Bytyqi, *et al.*, "Optimizing gravitational-wave detector design for squeezed light," Phys. Rev. D **105**, 102002 (2022).
47. A. Chernyshov, U. Sterr, F. Riehle, *et al.*, "Calibration of a Shack–Hartmann sensor for absolute measurements of wavefronts," Appl. Opt. **44**, 6419–6425 (2005).
48. C. Blair, Y. Levin, and E. Thrane, "Constraining temperature distribution inside LIGO test masses from frequencies of their vibrational modes," Phys. Rev. D **103**, 022003 (2021).
49. E. Morrison, D. I. Robertson, H. Ward, *et al.*, "Experimental demonstration of an automatic alignment system for optical interferometers," Appl. Opt. **33**, 5037–5040 (1994).
50. P. Fritschel, N. Mavalvala, D. Shoemaker, *et al.*, "Alignment of an interferometric gravitational wave detector," Appl. Opt. **37**, 6734–6747 (1998).
51. G. Mueller, Q. Ze Shu, R. Adhikari, *et al.*, "Determination and optimization of mode matching into optical cavities by heterodyne detection," Opt. Lett. **25**, 266–268 (2000).
52. F. Bayer-Helms, "Coupling coefficients of an incident wave and the modes of spherical optical resonator in the case of mismatching and misalignment," Appl. Opt. **23**, 1369–1380 (1984).
53. A. A. Ciobanu, D. D. Brown, P. J. Veitch, *et al.*, "Mode matching error signals using radio-frequency beam shape modulation," Appl. Opt. **59**, 9884–9895 (2020).
54. M. W. Beijersbergen, L. Allen, H. E. L. O. van der Veen, *et al.*, "Astigmatic laser mode converters and transfer of orbital angular momentum," Opt. Commun. **96**, 123–132 (1993).
55. J. Visser and G. Nienhuis, "Orbital angular momentum of general astigmatic modes," Phys. Rev. A **70**, 013809 (2004).
56. C. Bond, P. Fulda, and A. Freise, "Analytical calculation of Hermite-Gauss and Laguerre-Gauss modes on a bullseye photodiode," arXiv, arXiv:1606.01057 Technical report T1600189 (LIGO Scientific Collaboration, 2016). Available on arXiv e-prints: arXiv:1606.01057.
57. A. T. O'Neil and J. Courtial, "Mode transformations in terms of the constituent Hermite-Gaussian or Laguerre-Gaussian modes and the variable-phase mode converter," Opt. Commun. **181**, 35–45 (2000).
58. R. Uren, S. Beecher, C. R. Smith, *et al.*, "Method for generating high purity laguerre-gaussian vortex modes," IEEE J. Quantum Electron. **55**, 1700109 (2019).
59. F. Magana-Sandoval, T. Vo, D. Vander-Hyde, *et al.*, "Sensing optical cavity mismatch with a mode-converter and quadrant photodiode," Phys. Rev. D **100**, 102001 (2019).
60. F. Magana-Sandoval, S. Ballmer, T. Vo, *et al.*, "Mode converter and quadrant photodiode for sensing optical cavity mode mismatch," U.S. patent10,453,971 B2 (October 22, 2019).
61. A. Grimaldi, "Mode matching sensing frequency dependent squeezing source for Advanced Virgo plus," Ph.d. thesis (Universita di Trento, 2022).
62. P. Fulda, D. Voss, C. Mueller, *et al.*, "Alignment sensing for optical cavities using radio-frequency jitter modulation," Appl. Opt. **56**, 3879–3888 (2017).
63. H. Vahlbruch, S. Chelkowski, B. Hage, *et al.*, "Coherent control of vacuum squeezing in the gravitational-wave detection band," Phys. Rev. Lett. **97**, 011101 (2006).
64. S. Chelkowski, H. Vahlbruch, K. Danzmann, *et al.*, "Coherent control of broadband vacuum squeezing," Phys. Rev. A **75**, 043814 (2007).
65. D. Ganapathy, V. Xu, W. Jia, *et al.*, "Probing squeezing for gravitational-wave detectors with an audio-band field," Phys. Rev. D **105**, 122005 (2022).
66. M. Diaz-Ortiz and P. Fulda, "An electro-optic lens concept for mode mismatch sensing," in *Presented at the LIGO-Virgo-KAGRA Biannual Conference, Conference Presentation G2001575* (LIGO Scientific Collaboration, 2020).
67. M. Bazzan, M. Carlassara, G. Ciani, *et al.*, "Test of lg10 rf high order mode sensing techniquefor laser-cavity mode-matching," in *Presented at the LIGO-Virgo-KAGRA Biannual Conference, Conference Presentation LIGO-G2001619* (Virgo Scientific Collaboration, 2020).
68. G. Chiarini and G. Ciani, "Mode matching sensing through rf higher order modulation method," in *Gravitational-Wave Advanced Detector Workshop* (2023).
69. L. Tao, P. Fulda, and A. C. Green, "Misalignment and mode mismatch error signals for higher-order Hermite-Gauss modes from two sensing schemes," Phys. Rev. D **108**, 062001 (2023).
70. A. W. Goodwin-Jones, H. Zhu, C. Blair, *et al.*, "Single and coupled cavity mode sensing schemes using a diagnostic field," Opt. Exp. **31**, 35068–35085 (2023), .
71. A. W. Goodwin-Jones, "Coupled cavity pole and mode mismatch," LIGO Electronic Log 60763 (LIGO, 2022), available at https://alog.ligo-la.caltech.edu/aLOG/index.php?callRep=60763.
72. L. Pinard, C. Michel, B. Sassolas, *et al.*, "Mirrors used in the LIGO interferometers for first detection of gravitational waves," Appl. Opt. **56**, C11–C15 (2017).
73. S. Biscans, S. Gras, C. D. Blair, *et al.*, "Suppressing parametric instabilities in LIGO using low-noise acoustic mode dampers," Phys. Rev. D **100**, 122003 (2019).
74. J. Betzwieser, "Analysis of spatial mode sensitivity of a gravitational wave interferometer and a targeted search for gravitational radiation from the crab pulsar," Ph.d. thesis (Massachusetts Institute of Technology, 2007).
75. K. Goda, D. Ottaway, B. Connelly, *et al.*, "Frequency-resolving spatiotemporal wave-front sensor," Opt. Lett. **29**, 1452–1454 (2004).
76. J. Betzwieser, K. Kawabe, and L. Matone, "Study of the ouput mode cleaner prototype using the phasecamera," LIGO internal working note LIGO-T040156-00-D (2004).
77. A. Gretarsson, E. D'Ambrosio, V. Frolov, *et al.*, "Effects of mode degeneracy in the LIGO livingston observatory recycling cavity," J. Opt. Soc. Am. B **24**, 2821–2828 (2007).

78. K. Agatsuma, L. van der Schaaf, M. van Beuzekom, *et al.*, "High-performance phase camera as a frequency selective laser wavefront sensor for gravitational wave detectors," Opt. Express **27**, 18533–18548 (2019).
79. L. van der Schaaf, K. Agatsuma, M. van Beuzekom, *et al.*, "Advanced Virgo phase cameras," J. Phys. Conf. Ser. **718**, 072008 (2016).
80. H. T. Cao, D. D. Brown, P. J. Veitch, *et al.*, "Optical lock-in camera for gravitational wave detectors," Opt. Express **28**, 14405–14413 (2020).
81. D. Brown, H. T. Cao, P. Veitch, *et al.*, "Optical lock-in camera: Lho o3 results and imaging error signals," Tech. Rep. LIGO-G2001604 (LIGO Scientific Collaboration, 2020). Talk presented at LVK Conference Sep 2020.
82. M. Schiworski, V. Bossilkov, C. Blair, *et al.*, "Observing the optical modes of parametric instability," Opt. Lett. **47**, 1685–1688 (2022).
83. M. G. Schiworski, D. D. Brown, and D. J. Ottaway, "Modal decomposition of complex optical fields using convolutional neural networks," J. Opt. Soc. Am. A **38**, 1603–1611 (2021).
84. M. Hansard, S. Lee, O. Choi, *et al.*, *Time of Flight Cameras: Principles, Methods, and Applications*, Springer Briefs in Computer Science (2012).
85. T. V. Collaboration, "Advanced Virgo technical design report," Virgo technical report VIR-0128A-12 (2012).
86. E. Muñiz, V. Srivastava, S. Vidyant, *et al.*, "High frame-rate phase camera for high-resolution wavefront sensing in gravitational-wave detectors," Phys. Rev. D **104**, 042002 (2021).
87. D. T. Ralph, P. A. Altin, D. S. Rabeling, *et al.*, "Interferometric wavefront sensing with a single diode using spatial light modulation," Appl. Opt. **56**, 2353–2358 (2017).
88. R. Cabrita, "Sensing mode mismatch with the phase cameras at Advanced Virgo," in *Proceedings of the Gravitational-waves Science & Technology Symposium (GRASS)* (Zenodo, 2022).
89. N. Uehara, E. K. Gustafson, M. M. Fejer, *et al.*, "Modeling of efficient mode-matching and thermal-lensing effect on a laser-beam coupling into a mode-cleaner cavity," Proc. SPIE **2989**, 57–68 (1997).
90. P. Kwee, F. Seifert, B. Willke, *et al.*, "Laser beam quality and pointing measurement with an optical resonator," Rev. Sci. Instrum. **78**, 073103 (2007).
91. C. Bogan, P. Kwee, S. Hild, *et al.*, "Novel technique for thermal lens measurement in commonly used optical components," Opt. Express **23**, 15380–15389 (2015).
92. M. L. Mah and J. J. Talghader, "Decomposition of aberrated or turbulent wavefronts into a spatial mode spectrum using optical cavities," Appl. Opt. **58**, 4288–4299 (2019).
93. K. Takeno, N. Ohmae, N. Mio, *et al.*, "Determination of wavefront aberrations using a Fabry Pérot cavity," Opt. Commun. **284**, 3197–3201 (2011).
94. A. W. Jones, "Impact and mitigation of wavefront distortions in precision interferometry," Ph.d. thesis (The University of Birmingham, 2020).
95. A. W. Jones, M. Wang, C. M. Mow-Lowry, *et al.*, "High dynamic range spatial mode decomposition," Opt. Express **28**, 10253–10269 (2020).
96. M. A. Golub, A. M. Prokhorov, I. N. Sisakyan, *et al.*, "Synthesis of spatial filters for investigation of the transverse mode composition of coherent radiation," Sov. J. Quantum Electron. **12**, 1208–1209 (1982).
97. A. Forbes, A. Dudley, and M. McLaren, "Creation and detection of optical modes with spatial light modulators," Adv. Opt. Photon. **8**, 200–227 (2016).
98. J. A. Davis, D. M. Cottrell, J. Campos, *et al.*, "Encoding amplitude information onto phase-only filters," Appl. Opt. **38**, 5004–5013 (1999).
99. B. R. Boruah, "Dynamic manipulation of a laser beam using a liquid crystal spatial light modulator," Am. J. Phys. **77**, 331–336 (2009).
100. D. Flamm, D. Naidoo, C. Schulze, *et al.*, "Mode analysis with a spatial light modulator as a correlation filter," Opt. Lett. **37**, 2478–2480 (2012).
101. E. Bolduc, N. Bent, E. Santamato, *et al.*, "Exact solution to simultaneous intensity and phase encryption with a single phase-only hologram," Opt. Lett. **38**, 3546–3549 (2013).
102. T. Kaiser, D. Flamm, S. Schröter, *et al.*, "Complete modal decomposition for optical fibers using CGH-based correlation filters," Opt. Express **17**, 9347–9356 (2009).
103. V. Soifer and M. Golub, *Laser Beam Mode Selection by Computer Generated Holograms* (CRC Press, 1994).
104. A. W. Jones, M. Wang, X. Zhang, *et al.*, "Metasurface-enhanced spatial mode decomposition," Phys. Rev. A **105**, 053523 (2022).
105. L. McCuller, "Beam layout requirements imposed by wavefront actuators," LIGO document T1900144 (LIGO, 2019).
106. D. Alaluf, R. Bastaits, K. Wang, *et al.*, "Unimorph mirror for adaptive optics in space telescopes," Appl. Opt. **57**, 3629–3638 (2018).
107. R. Cousty, T. Antonini, M. Aubry, *et al.*, "Monomorph deformable mirrors: from ground-based facilities to space telescopes," Proc. SPIE **10562**, 1056231 (2017).
108. S. G. Alcock, J. P. Sutter, K. J. Sawhney, *et al.*, "Bimorph mirrors: the good, the bad, and the ugly," Nucl. Instrum. Methods Phys. Res., Sect. A **710**, 87–92 (2013).
109. A. Kudryashov, A. Alexandrov, A. Rukosuev, *et al.*, "Extremely high-power CO_2 laser beam correction," Appl. Opt. **54**, 4352–4358 (2015).
110. K. L. Wlodarczyk, E. Bryce, N. Schwartz, *et al.*, "Scalable stacked array piezoelectric deformable mirror for astronomy and laser processing applications," Rev. Sci. Instrum. **85**, 024502 (2014).
111. V. Samarkin, A. Alexandrov, G. Borsoni, *et al.*, "Wide aperture piezoceramic deformable mirrors for aberration correction in high-power lasers," High Power Laser Sci. Eng. **4**, e4 (2016).
112. R. Lawrence, M. Zucker, P. Fritschel, *et al.*, "Adaptive thermal compensation of test masses in advanced LIGO," Classical Quantum Gravity **19**, 1803–1812 (2002).
113. H. Lück, A. Freise, S. Goßler, *et al.*, "Thermal correction of the radii of curvature of mirrors for geo 600," Classical Quantum Gravity **21**, S985–S989 (2004).
114. I. Nardecchia, Y. Minenkov, M. Lorenzini, *et al.*, "Optimized radius of curvature tuning for the Virgo core optics," Classical Quantum Gravity **40**, 055004 (2023).
115. L. Aiello, E. Cesarini, V. Fafone, *et al.*, "Thermal compensation system in advanced and third generation gravitational wave interferometric detectors," J. Phys. Conf. Ser. **1226**, 012019 (2019).
116. A. Brooks, "Sr3 heater actuator update," LIGO document G1501373 (LIGO, 2015).
117. H. T. Cao, R. Anderson, T. Rosauer, *et al.*, "Development status of hom ring heater," in *Presented at the LIGO-Virgo-KAGRA Biannual Conference, Conference Presentation LIGO-G2201439* (LIGO Scientific Collaboration, 2022).
118. T. Accadia, F. Acernese, M. Agathos, *et al.*, "Central heating radius of curvature correction (CHROCC) for use in large scale gravitational wave interferometers," Classical Quantum Gravity **30**, 055017 (2013).
119. J. Degallaix, C. Zhao, L. Ju, *et al.*, "Thermal lensing compensation for AIGO high optical power test facility," Classical Quantum Gravity **21**, S903 (2004).
120. C. Zhao, J. Degallaix, L. Ju, *et al.*, "Compensation of strong thermal lensing in high-optical-power cavities," Phys. Rev. Lett. **96**, 231101 (2006).
121. G. Mueller, R. S. Amin, D. Guagliardo, *et al.*, "Method for compensation of thermally induced modal distortions in the input optical components of gravitational wave interferometers," Classical Quantum Gravity **19**, 1793 (2002).
122. O. V. Palashov, D. S. Zheleznov, A. V. Voitovich, *et al.*, "High-vacuum-compatible high-power Faraday isolators for gravitational-wave interferometers," J. Opt. Soc. Am. B **29**, 1784–1792 (2012).
123. C. L. Mueller, M. A. Arain, G. Ciani, *et al.*, "The advanced LIGO input optics," Rev. Sci. Instrum. **87**, 014502 (2016).
124. C. Zhao, M013, The University of Western Australia, 35 Stirling Hwy, Perth, Australia (personal communication, 2023).
125. J. Degallaix, B. Slagmolen, C. Zhao, *et al.*, "Thermal lensing compensation principle for the Aciga's high optical power test facility test 1," Gen. Relativ. Gravit. **37**, 1581–1589 (2005).
126. C. Blair, M013, The University of Western Australia, 35 Stirling Hwy, Perth, Australia (personal communication, 2023).
127. G. Billingsley, "Advanced LIGO thin compensation plate," LIGO document E1000158 (LIGO, 2010).
128. G. Billingsley, "Customized polish for advanced LIGO thin compensation plate," LIGO document E1400394-v3 (LIGO, 2015).
129. M. L., "Realization and characterization of a scanning system for optical asymmetric aberrations in Advanced Virgo," Master thesis (University of Rome Tor Vergata, 2013).
130. C. Taranto, E. Cesarini, M. Cifaldi, *et al.*, "Mitigation of non-axisymmetric optical aberrations in Advanced Virgo Plus," in *Presented at the GWADW23 Conference, Conference Presentation VIR-0373A-23* (VIRGO Scientific Collaboration, 2023).
131. S. Mehrabkhani and M. Kuester, "Optimization of phase retrieval in the Fresnel domain by the modified Gerchberg-Saxton algorithm," arXiv, arXiv:1711.01176 (2017).

132. R. A. Day, G. Vajente, M. Kasprzack, *et al.*, "Reduction of higher order mode generation in large scale gravitational wave interferometers by central heating residual aberration correction," Phys. Rev. D **87**, 082003 (2013).
133. G. Vajente, "In situ correction of mirror surface to reduce round-trip losses in Fabry-Perot cavities," Appl. Opt. **53**, 1459–1465 (2014).
134. H. Wittel, C. Affeldt, A. Bisht, *et al.*, "Matrix heater in the gravitational wave observatory geo 600," Opt. Express **26**, 22687–22697 (2018).
135. M. C. E. Cesarini, V. Fafone, M. Lorenzini, *et al.*, "Mitigation of point absorbers in the Advanced Virgo Plus core optics: the actuator design," in *GWADW23 Conference presentation, VIRGO Scientific Collaboration* (2023).
136. M. C. E. Cesarini, V. Fafone, M. Lorenzini, *et al.*, "Mitigation of point absorbers in the Advanced Virgo Plus core optics: the actuator design," in *Conference presentation* (VIRGO Scientific Collaboration, 2022).
137. A. F. Brooks, G. Vajente, H. Yamamoto, *et al.*, "Point absorbers in advanced LIGO," Appl. Opt. **60**, 4047–4063 (2021).
138. M. Arain, "Adaptive thermal compensation for the input optics of advanced LIGO," LIGO document G0900115-v2 (LIGO, 2009).
139. P. F. G. Mueller and Z. Liu, "Adaptive optical element," LIGO document G1200866 (LIGO, 2012).
140. Z. Liu, M. Arain, L. Williams, *et al.*, "Prototyping the io adaptive optical element in advanced LIGO," LIGO document G1100359 (LIGO, 2011).
141. P. Fulda, Department of Physics, The University of Florida, 2001 Museum Rd, Gainesville, FL 32611, United States (personal communication, 2023).
142. M. A. Arain, W. Z. Korth, L. F. Williams, *et al.*, "Adaptive control of modal properties of optical beams using photothermal effects," Opt. Express **18**, 2767–2781 (2010).
143. B. Canuel, R. Day, E. Genin, *et al.*, "Wavefront aberration compensation with a thermally deformable mirror," Classical Quantum Gravity **29**, 085012 (2012).
144. M. Kasprzack, B. Canuel, F. Cavalier, *et al.*, "Performance of a thermally deformable mirror for correction of low-order aberrations in laser beams," Appl. Opt. **52**, 2909–2916 (2013).
145. D. Ganapathy, W. Jia, M. Nakano, *et al.*, "Broadband quantum enhancement of the LIGO detectors with frequency-dependent squeezing," Phys. Rev. X **13**, 041021 (2023).
146. L. McCuller, S. E. Dwyer, A. C. Green, *et al.*, "LIGO's quantum response to squeezed states," Phys. Rev. D **104**, 062006 (2021).
147. D. Töyrä, D. D. Brown, M. Davis, *et al.*, "Multi-spatial-mode effects in squeezed-light-enhanced interferometric gravitational wave detectors," Phys. Rev. D **96**, 022006 (2017).
148. H. T. Cao, A. Brooks, S. W. S. Ng, *et al.*, "High dynamic range thermally actuated bimorph mirror for gravitational wave detectors," Appl. Opt. **59**, 2784–2790 (2020).
149. A. W. Goodwin-Jones and H. T. Cao, are preparing a manuscript to be called "Large diameter thermally actuated deformable mirrors for 3rd generation gravitational wave detectors,".
150. V. Srivastava, G. Mansell, C. Makarem, *et al.*, "Piezo-deformable mirrors for active mode matching in advanced LIGO," Opt. Express **30**, 10491–10501 (2022).
151. J.-Y. Vinet, "On special optical modes and thermal issues in advanced gravitational wave interferometric detectors," Living Rev. Relativity **12**, 1–123 (2009).
152. S. J. Cooper, C. M. Mow-Lowry, D. Hoyland, *et al.*, "Sensors and actuators for the advanced LIGO A+ upgrade," Rev. Sci. Instrum. **94**, 014502 (2023).
153. K. Kokeyama, K. Izumi, W. Z. Korth, *et al.*, "Residual amplitude modulation in interferometric gravitational wave detectors," J. Opt. Soc. Am. A **31**, 81–88 (2014).
154. L. van der Schaaf, "The phase cameras of Advanced Virgo," Ph.D. thesis (Nikhef, Vrije Universiteit, 2020).
155. D. Reitze, R. X. Adhikari, S. Ballmer, *et al.*, "Cosmic explorer: the U.S. contribution to gravitational-wave astronomy beyond LIGO," Bull. Am. Astron. Soc. **51**, 35 (2019).
156. C. Simon, "Towards a global quantum network," Nat. Photonics **11**, 678–680 (2017).
157. C. A. Casacio, L. S. Madsen, A. Terrasson, *et al.*, "Quantum-enhanced nonlinear microscopy," Nature **594**, 201–206 (2021).
158. C. Lisdat, G. Grosche, N. Quintin, *et al.*, "A clock network for geodesy and fundamental science," Nat. Commun. **7**, 12443 (2016).
159. R. X. Adhikari, K. Arai, A. F. Brooks, *et al.*, "A cryogenic silicon interferometer for gravitational-wave detection," Classical Quantum Gravity **37**, 165003 (2020).
160. A. Utina, A. Amato, J. Arends, *et al.*, "ETpathfinder: a cryogenic testbed for interferometric gravitational-wave detectors," Classical Quantum Gravity **39**, 215008 (2022).
161. A. Sider, L. Amez-Droz, A. Amorosi, *et al.*, "E-TEST prototype design report," arXiv, arXiv:2212.10083 (2022).
162. R. Adhikari, S. Appert, K. Arai, *et al.*, "Mariner: the cryogenic upgrade of the 40m prototype interferometer," in *Presented at the GWADW23 Conference, Conference Presentation G2301014* (LIGO Scientific Collaboration, 2023).
163. A. W. Goodwin-Jones, A. Al-Jodah, H. C. J. Winterflood, *et al.*, "Towards a nemo prototype," in *Presented at the GWADW23 Conference, Conference Presentation LIGO-G2301023* (LIGO Scientific Collaboration, 2023).
164. F. Acernese, M. Agathos, A. Ain, *et al.*, "Advanced Virgo Plus: Future perspectives," J. Phys. Conf. Ser. **2429**, 012040 (2023).
165. P. Fritschel, K. Kuns, J. Driggers, *et al.*, "Report of the LSC post-05 study group," Tech. Rep. LIGO T2200287 (LIGO Scientific Collaboration, 2022).
166. V. Fafone and S. Nissanke, "Virgo_nEXT: beyond the AdV+ project: a concept study of the LSC post-05 study group," Tech. Rep. VIR-0617A-22 (Virgo Scientific Collaboration, 2022), available at https://indico.ego-gw.it/event/457/contributions/3835/attachments/2102/3748/220613_Fafone-Nissanke_PO5_Council_upload.pdf.
167. J. Liu, V. Bossilkov, C. Blair, *et al.*, "Angular instability in high optical power suspended cavities," Rev. Sci. Instrum. **89**, 124503 (2018).
168. M. Evans, S. Gras, P. Fritschel, *et al.*, "Observation of parametric instability in advanced LIGO," Phys. Rev. Lett. **114**, 161102 (2015).
169. J. Pan, J. Zhang, C. Blair, *et al.*, "Parametric instability in the neutron star extreme matter observatory," Classical Quantum Gravity **39**, 085007 (2022).
170. K. Ramirez, "Lockloss at 00:50 UTC due to PI," LIGO Electronic Log 65817 (LIGO, 2023), available at https://alog.ligo-la.caltech.edu/aLOG/index.php?callRep=65817.
171. E. Capote, "Advanced LIGO detector commissioning for O4," Conference Presentation LIGO G2301034 (LIGO Scientific Collaboration, 2023), available at https://agenda.infn.it/event/32907/contributions/200466/attachments/105441/148241/GWADW2023.pptx.
172. V. Frolov, "Mich/srcl/asc injections for darm noise budget," LIGO Electronic Log 64807 (LIGO, 2023), available at https://alog.ligo-la.caltech.edu/aLOG/index.php?callRep=64807.
173. V. Bossilkov, "Arm asc hard loop compensation for 60w input," LIGO Electronic Log 64243 (LIGO, 2023), available at https://alog.ligo-la.caltech.edu/aLOG/index.php?callRep=64243.
174. H. T. Cao, A. Brooks, K. Kuns, *et al.*, "Post-05 thermal modeling A# TCS requirements status of HOM ring heater," in *Presented at the LIGO-Virgo-KAGRA Biannual Conference, Conference Presentation LIGO-G2300624* (LIGO Scientific Collaboration, 2023).
175. C. J. Glassbrenner and G. A. Slack, "Thermal conductivity of silicon and germanium from 3°k to the melting point," Phys. Rev. **134**, A1058–A1069 (1964).
176. P. Combis, P. Cormont, L. Gallais, *et al.*, "Evaluation of the fused silica thermal conductivity by comparing infrared thermometry measurements with two-dimensional simulations," Appl. Phys. Lett. **101**, 211908 (2012).
177. K. L. Wray and T. J. Connolly, "Thermal conductivity of clear fused silica at high temperatures," J. Appl. Phys. **30**, 1702–1705 (2004).
178. P. G. Klemens, "Thermal conductivity of pure monoisotopic silicon," Int. J. Thermophys. **2**, 323–330 (1981).
179. J. Eichholz, N. A. Holland, V. B. Adya, *et al.*, "Practical test mass and suspension configuration for a cryogenic kilohertz gravitational wave detector," Phys. Rev. D **102**, 122003 (2020).
180. H. J. Kimble, Y. Levin, A. B. Matsko, *et al.*, "Conversion of conventional gravitational-wave interferometers into quantum nondemolition interferometers by modifying their input and/or output optics," Phys. Rev. D **65**, 022002 (2001).
181. L. McCuller, C. Whittle, D. Ganapathy, *et al.*, "Frequency-dependent squeezing for advanced LIGO," Phys. Rev. Lett. **124**, 171102 (2020).
182. Y. Zhao, N. Aritomi, E. Capocasa, *et al.*, "Frequency-dependent squeezed vacuum source for broadband quantum noise reduction

in advanced gravitational-wave detectors," Phys. Rev. Lett. **124**, 171101 (2020).
183. F. Acernese, M. Agathos, A. Ain, *et al.*, "Frequency-dependent squeezed vacuum source for the Advanced Virgo gravitational-wave detector," Phys. Rev. Lett. **131**, 041403 (2023).
184. P. Kwee, J. Miller, T. Isogai, *et al.*, "Decoherence and degradation of squeezed states in quantum filter cavities," Phys. Rev. D **90**, 062006 (2014).
185. M. Punturo, "Einstein gravitational wave telescope conceptual design study," Tech. Rep. ET-0106C-10 (ET Science Team, 2010).
186. P. Jones, T. Zhang, H. Miao, *et al.*, "Implications of the quantum noise target for the Einstein Telescope infrastructure design," Phys. Rev. D **101**, 082002 (2020).
187. S. Steinlechner, N.-O. Rohweder, M. Korobko, *et al.*, "Mitigating mode-matching loss in nonclassical laser interferometry," Phys. Rev. Lett. **121**, 263602 (2018).
188. V. J. Hamedan, C. Blair, J. Liu, *et al.*, "Preventing transient parametric instabilities in high power gravitational wave detectors using thermal transient compensation," Classical Quantum Gravity **34**, 145014 (2017).
189. V. J. Hamedan, C. Zhao, L. Ju, *et al.*, "Suppression of thermal transients in advanced LIGO interferometers using CO_2 laser preheating," Classical Quantum Gravity **35**, 115006 (2018).
190. H.-S. Zhong, H. Wang, Y.-H. Deng, *et al.*, "Quantum computational advantage using photons," Science **370**, 1460–1463 (2020).
191. L. S. Madsen, F. Laudenbach, M. F. Askarani, *et al.*, "Quantum computational advantage with a programmable photonic processor," Nature **606**, 75–81 (2022).
192. S. Takeda and A. Furusawa, "Toward large-scale fault-tolerant universal photonic quantum computing," APL Photon. **4**, 060902 (2019).
193. K. Fukui and S. Takeda, "Building a large-scale quantum computer with continuous-variable optical technologies," J. Phys. B **55**, 012001 (2022).
194. T. Kashiwazaki, T. Yamashima, K. Enbutsu, *et al.*, "Over-8-db squeezed light generation by a broadband waveguide optical parametric amplifier toward fault-tolerant ultra-fast quantum computers," Appl. Phys. Lett. **122**, 234003 (2023).
195. S. Pirandola, U. L. Andersen, L. Banchi, *et al.*, "Advances in quantum cryptography," Adv. Opt. Photon. **12**, 1012–1236 (2020).
196. Y. Wang, X. Wu, L. Zhang, *et al.*, "Performance improvement of free-space continuous-variable quantum key distribution with an adaptive optics unit," Quantum Inf. Process. **18**, 251 (2019).
197. D. J. Richardson, J. M. Fini, and L. E. Nelson, "Space-division multiplexing in optical fibres," Nat. Photonics **7**, 354–362 (2013).
198. A. Wang, L. Zhu, L. Wang, *et al.*, "Directly using 8.8-km conventional multi-mode fiber for 6-mode orbital angular momentum multiplexing transmission," Opt. Express **26**, 10038–10047 (2018).
199. A. W. Jones and A. Freise, "Increased sensitivity of higher-order laser beams to mode mismatches," Opt. Lett. **45**, 5876–5878 (2020).
200. X. Y. Zeng, Y. X. Ye, X. H. Shi, *et al.*, "Thermal-noise-limited higher-order mode locking of a reference cavity," Opt. Lett. **43**, 1690–1693 (2018).
201. D. Jiao, J. Gao, X. Deng, *et al.*, "Sub-hertz frequency stabilization of 1.55 μm laser on higher order HGMN mode," Opt. Commun. **463**, 125460 (2020).
202. M. Dovale-Álvarez, D. Brown, A. Jones, *et al.*, "Fundamental limitations of cavity-assisted atom interferometry," Phys. Rev. A **96**, 053820 (2017).
203. B. Canuel, A. Bertoldi, L. Amand, *et al.*, "Exploring gravity with the miga large scale atom interferometer," Sci. Rep. **8**, 14064 (2018).
204. M. Mestre, B. F. Diry, V. de Lesegno, *et al.*, "Cold atom guidance by a holographically-generated Laguerre-Gaussian laser mode," Eur. Phys. J. D **57**, 87–94 (2010).
205. M. I. Kolobov and C. Fabre, "Quantum limits on optical resolution," Phys. Rev. Lett. **85**, 3789 (2000).
206. K. Wagner, J. Janousek, V. Delaubert, *et al.*, "Entangling the spatial properties of laser beams," Science **321**, 541–543 (2008).
207. N. Treps, N. Grosse, W. P. Bowen, *et al.*, "A quantum laser pointer," Science **301**, 940–943 (2003).
208. L. Zhang, V. Boyer, M. Scully, *et al.*, "Quadrature squeezing of 10^4 spatial modes via manipulation of diffraction," Phys. Rev. A **105**, 023725 (2022).
209. Z. Li, H. Guo, H. Liu, *et al.*, "Higher-order spatially squeezed beam for enhanced spatial measurements," Adv. Quantum Technol. **5**, 2200055 (2022).
210. J. Heinze, B. Willke, and H. Vahlbruch, "Observation of squeezed states of light in higher-order Hermite-Gaussian modes with a quantum noise reduction of up to 10 db," Phys. Rev. Lett. **128**, 083606 (2022).
211. C. Embrey, M. Turnbull, P. Petrov, *et al.*, "Observation of localized multi-spatial-mode quadrature squeezing," Phys. Rev. X **5**, 031004 (2015).
212. C. Gabaldon, P. Barge, S. L. Cuozzo, *et al.*, "Quantum fluctuations spatial mode profiler," AVS Quantum Sci. **5**, 025005 (2023).
213. M. A. Taylor, J. Janousek, V. Daria, *et al.*, "Biological measurement beyond the quantum limit," Nat. Photon. **7**, 229–233 (2013).
214. M. Tsang, R. Nair, and X.-M. Lu, "Quantum theory of superresolution for two incoherent optical point sources," Phys. Rev. X **6**, 031033 (2016).
215. M. Tsang, "Subdiffraction incoherent optical imaging via spatial-mode demultiplexing," New J. Phys. **19**, 023054 (2017).